



New perspectives on the formation of the Boulder Bed of the western Bushveld Complex, South Africa

W. D. Smith^{1,2} · W. D. Maier¹ · D. D. Muir¹ · J. C. Ø. Andersen³ · B. J. Williams¹ · H. Henry⁴

Received: 25 December 2021 / Accepted: 24 October 2022 / Published online: 12 November 2022
© The Author(s), under exclusive licence to Springer-Verlag GmbH Germany, part of Springer Nature 2022

Abstract

The Boulder Bed of the western Bushveld Complex is an m-scale unit of mottled anorthosite containing sub-circular dm-scale ‘boulders’ of pyroxenite, harzburgite, or norite. To better understand this unit, we have combined high-resolution element mapping and electron back-scatter diffraction analysis with electron-probe microanalysis of plagioclase crystals from the boulders and their host anorthosite. Several key features pertinent to understanding the formation of this unit have been described, including (i) anhedral olivine is concentrated at the base of boulders, whereas clinopyroxene is concentrated towards the tops; (ii) the upward decrease in grain size through the boulders; (iii) the occurrence of chromite along the base of boulders and seldom along the top; (iv) the presence of strongly reverse-zoned cumulus plagioclase (An₇₅₋₉₅) in the so-called marginal zone underlying boulders; (v) the absence of deformation in the host anorthosite but the prevalence of intra-crystalline deformation in intercumulus pyroxene of the marginal zone; (vi) that amphibole (\pm apatite \pm phlogopite) partially line the base of some boulders; (vii) traces of pyrrhotite (\pm pentlandite \pm chalcopyrite) occur within the lower halves of boulders. We propose that the boulders formed in response to the disaggregation of a locally PGE-rich pyroxenite, triggered by heat- and (or) volatile-induced partial melting of the noritic host rocks. Several of the petrologic features arose from the reaction between the boulders and the noritic partial melt prior to late-stage viscous compaction.

Keywords Bushveld Complex · Boulder Bed · PGE · Merensky Reef · South Africa · EPMA · EBSD

Editorial handling: M. Fiorentini

Highlights

- Microtextural characterisation of the Boulder Bed of the Bushveld Complex.
- Strongly reverse-zoned plagioclase beneath boulders.
- Little evidence for microscopic deformation.
- A new petrogenetic model for the formation of the Boulder Bed.

✉ W. D. Smith
williamsmith3@cunet.carleton.ca

- ¹ School of Earth & Environmental Sciences, Cardiff University, Cardiff CF10 3AT, UK
- ² Department of Earth Sciences, Carleton University, 1125 Colonel By Drive, Ottawa, ON K1S 5B6, Canada
- ³ Camborne School of Mines, University of Exeter, Penryn, Exeter TR10 9EZ, UK
- ⁴ Géosciences Environment Toulouse, Toulouse University, CNRS, 14 Avenue E. Belin, 31400 Toulouse, IRD, France

Introduction

The ~2.056 Ga Bushveld Complex of South Africa is the largest known layered intrusion on Earth (Fig. 1A; Eales and Cawthorn 1996; Kinnaird 2005; Smith and Maier 2021). It comprises a ~6–8-km-thick sequence of mafic and ultramafic cumulate rocks, named the Rustenburg Layered Suite, that hosts most of the world’s platinum-group element (PGE), Cr, and V resources, as well as substantial Ni and Cu resources (Cawthorn 2015). The stratigraphy of the Rustenburg Layered Suite has been divided into the marginal, lower, critical, main, and upper zones (Hall 1924). Stratiform PGE mineralised reefs mostly occur at the base of the so-called cyclic units in the upper critical zone, including the Merensky Reef and the UG2 chromitite. Elevated PGE concentrations (mostly 50–70 ppb but reaching several ppm in places) are also reported from the enigmatic Boulder Bed (Vermaak 1976; Maier and Barnes 2003; Naldrett et al. 2009), which exclusively occurs in the western lobe of the Bushveld Complex (Fig. 1A).

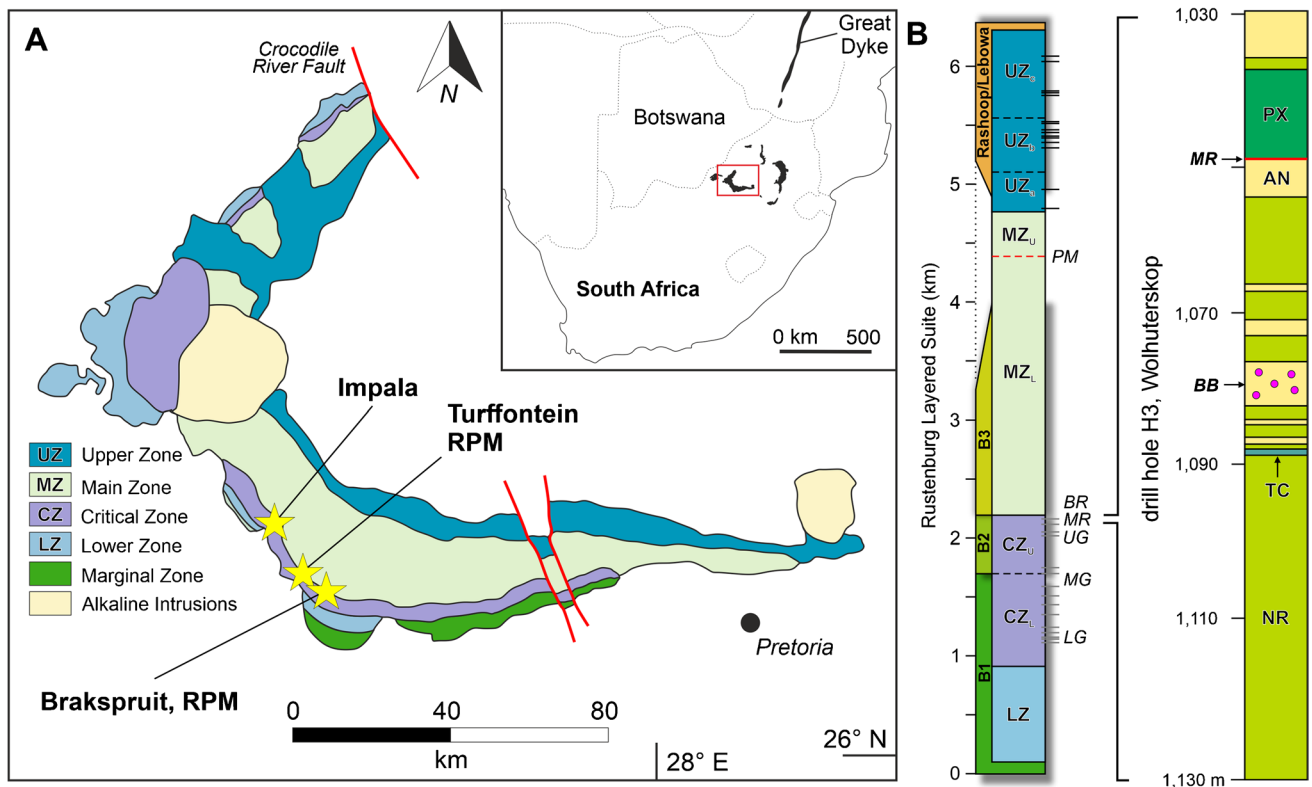


Fig. 1 **A** Geological map of the western lobe of the Bushveld Complex (modified from Yao and Mungall 2021), highlighting locations of samples acquired for this study. RPM = Rustenburg Platinum Mine. **B** Stratigraphic section of the Bushveld Complex (modified from Yao

and Mungall 2021) and the upper critical zone from drill hole H3 at Wolhuterskop (modified from Maier and Eales 1997). Note the location of the Boulder Bed (BB) below the Merensky Reef (MR). Abbreviations: NR, norite; TC, troctolite; AN, anorthosite; PX, pyroxenite

The Boulder Bed is an unusual unit of mottled anorthosite located 10 s of metres below the Merensky Reef that contains sub-circular pyroxenitic-harzburgitic aggregates known as ‘boulders’ (Jones 1976; Maier and Eales 1997). At the Impala and Rustenburg mines, the unit is generally 1 to 5 m in thickness. The boulders are not randomly distributed but rather occur along planar horizons in the host anorthosite. The boulders typically range from 5 to 20 cm in diameter and consistently display a ‘right-way up’ architecture, i.e. olivine is concentrated at the base and clinopyroxene is concentrated at the top (Jones 1976; Lee and Sharpe 1980). Chromite crystals irregularly line the lower and upper surfaces of boulders, and in places, extend laterally from boulders into the host rocks as stringer veins (Maier and Barnes 2003). In many cases, the boulders are partially rimmed by a thin corona of pure plagioclase, which in turn is rimmed by a ~ 1-cm-thick noritic to gabbronoritic margin.

Several authors have likened the boulders to the central pyroxenite of the Merensky Reef, citing their coarse-grain size relative to the host rocks, their association with chromite and anorthosite, and their comparable whole-rock and mineral compositions (Vermaak 1976; Lee and Sharpe 1980; Maier and Barnes 2003). As such, several models have been

proposed for the formation of the boulders, including crystallisation from trapped intercumulus melts (Ferguson and Botha 1963; Vermaak 1976) or recrystallisation following the break-up of a preexisting mafic–ultramafic unit (Jones 1976; Maier and Barnes 2003). In the present study, we present high-resolution element maps of some boulders together with plagioclase compositions and electron back-scattered diffraction (EBSD) maps to test the proposed petrogenetic models for the Boulder Bed and reveal insights into the formation of other enigmatic units in the upper critical zone, namely the Merensky Reef and Pseudoreefs.

Summary of previous work on the Boulder Bed

Lithological and petrological descriptions of the Boulder Bed and its host rocks have been given by several authors (Ferguson and Botha 1963; Cousins 1969; Vermaak 1976; Jones 1976; Lee and Sharpe 1980; Viljoen and Hieber 1986; Naldrett et al. 1986; Leeb-Du Toit 1986; Maier and Eales 1997; Maier and Barnes 2003). At the Impala and Rustenburg mines, where the boulders are most common,

the Boulder Bed is a 1- to 5-m-thick interval of mottled anorthosite that occurs 20–60 m below the Merensky Reef (Fig. 1B; Maier and Barnes 2003). The unit contains sub-circular ‘boulders’ of (olivine)-pyroxenite, harzburgite, or norite, which variably contain subhedral to anhedral orthopyroxene (Mg_{73-83}), anhedral olivine (Fo_{82-91}), plagioclase (An_{71-79}), and clinopyroxene (Mg_{76-84}), as well as minor amounts of chromite, quartz, apatite, and sulfide (primarily pyrrhotite; Lee and Sharpe 1980; Maier and Eales 1997; Maier and Barnes 2003).

Olivine and accessory sulfides are concentrated in the lower portion of boulders, whereas plagioclase and clinopyroxene are often concentrated in the upper portion (Vermaak 1967; Maier and Barnes 2003). Approximately two-thirds of boulders possess thin (< 1 cm) chromite selvages along their basal surface, which in some cases extend laterally into the host rock (see Fig. 2C of Maier and Barnes 2003; Leeb-Du Toit 1986). Boulders seldom display chromite selvages along their upper surface. Amphibole, chlorite, and Mg-mica are found along the base of some 20% of boulders, and more

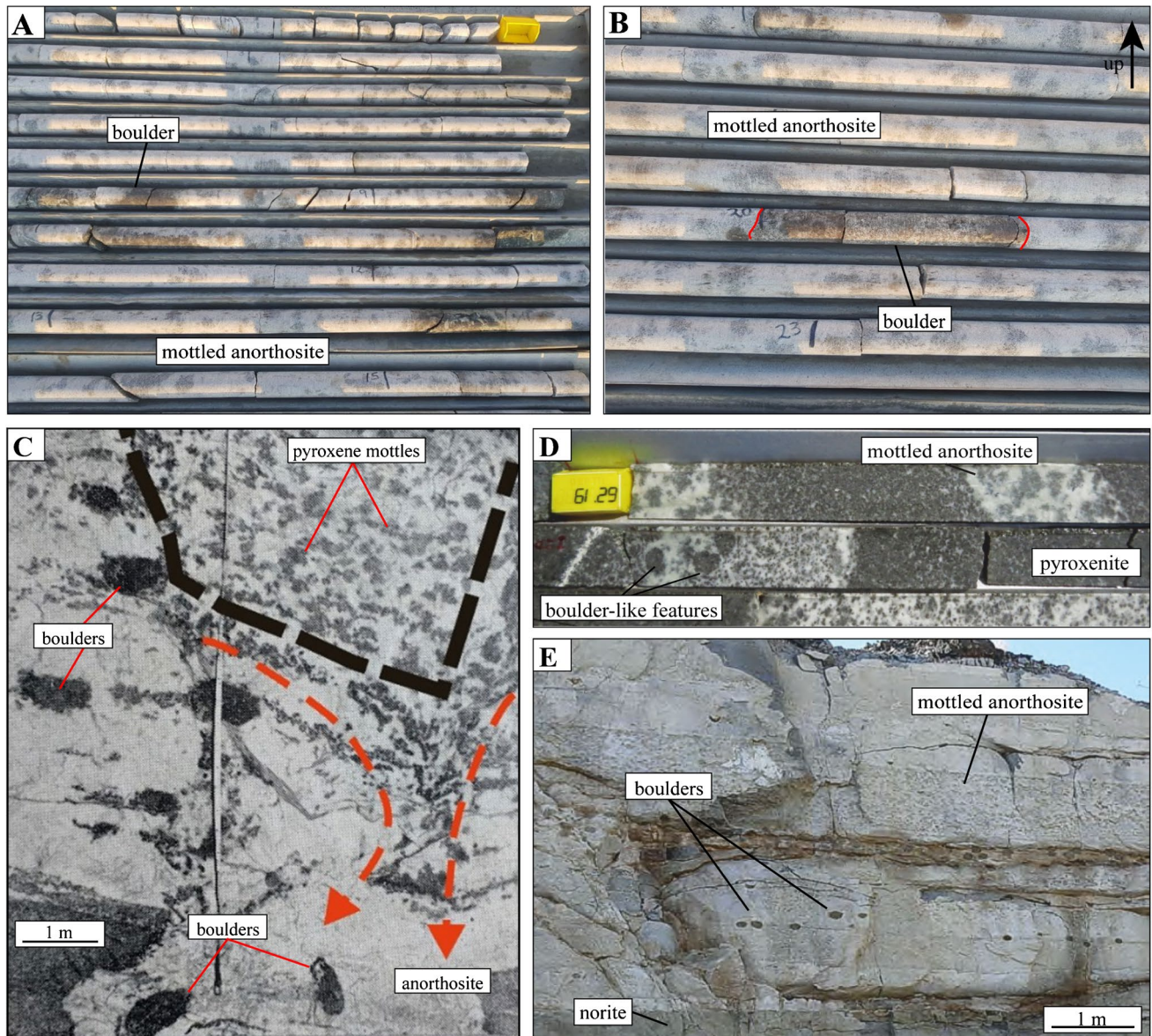


Fig. 2 **A, B** Photographs of the Boulder Bed (Footwall 6) in drill core sampled from the Impala 16# shaft. **C** Fig. 16 from Viljoen and Hieber (1986) shows an example of slumping of the Boulder Bed (host anorthosite and pyroxenitic boulders) into the footwall. **D** Comparable pyroxenitic boulders hosted in anorthosite of the Bastard Reef

in the northern limb of the Bushveld Complex. **E** The occurrence of pyroxenitic ‘boulders’ in mottled anorthosite bracketed by norite at the Lonmin Marikana UG2 pit. The mottled anorthosite unit has been partially intruded by an iron-rich ultramafic pegmatite (pictures provided by D. Reid)

rarely, along their upper contacts (Vermaak 1976; Maier and Barnes 2003).

Orthopyroxene and plagioclase within boulders are less compositionally evolved than those in the host anorthosite yet comparable in composition to those of the Merensky footwall norite (Jones 1976; Maier and Eales 1997). Jones (1976) recorded reverse zoning in cumulus plagioclase crystals in the host anorthosite (An_{76-80}), a feature that has been observed in mottled anorthosite elsewhere in the upper Critical Zone (Maier and Eales 1997; Maier et al. 2021). The composition of chromite crystals in and around the boulders ($Cr/Fe=0.63-1.23$, $Cr/Al=1.35-2.8$, and $Mg\#=0.26-0.29$; Maier and Eales 1997) is comparable to those in the bracketing noritic rocks but more evolved than those in Critical Zone chromitite seams.

The boulders are broadly circular in plan (average diameter of 225 ± 40 mm; e.g. Cousins 1969) and flattened in section (average thickness of 105 mm; Lee and Sharpe 1980). Their long axis is oriented mostly sub-parallel to the lithologic layering (Cousins 1969; Jones 1976). Their lower surface tends to be more convex than their upper surface (Lee and Sharpe 1980). The boulders are coarse-grained (Lee and Sharpe 1980; Maier and Barnes 2003), yet their grain size generally decreases upward and towards their margins (Vermaak 1976). Contacts between boulders and the host anorthosite can be knife-sharp (Cousins 1969) or diffuse (Fig. 2A, B). Some boulders are surrounded by so-called ‘bleached zones’ of anorthosite that can range from several mm to ≥ 1 cm in thickness (Ferguson and Botha 1963; Jones 1976). Somewhat analogous features have been described in

anorthosite and leuconorite within the Merensky-UG2 interval, whereby ‘micro-boulders’ of monomineralic anorthosite are cored by intercumulus pyroxene and sometimes olivine (Maier 1995; Maier and Eales 1997; Maier et al. 2021). Viljoen and Hieber (1986) have reported evidence for macroscopic deformation of the Boulder Bed, showing boulders slumping transversely into their noritic footwall, producing a pothole (Fig. 2C).

There are relatively few published whole-rock compositional data for the Boulder Bed (Jones 1976; Lee and Sharpe 1980; Naldrett et al. 1986; Maier and Barnes 2003). The major element composition of the boulders is comparable to that of the Merensky coarse-grained pyroxenite (18.7–22.2 wt.% MgO and 5.2–8.1 wt.% CaO), yet with relatively lower, albeit highly variable S ($\sim 230-18,000$ ppm) and chalcophile element ($\sim 50-70,000$ ppb PGE, $\sim 12-3000$ ppm Cu, and $\sim 400-8500$ ppm Ni) concentrations (Jones 1976; Lee and Sharpe 1980; Maier and Barnes 2003). The trace element concentrations (including rare earth elements) are comparable to those of the Merensky footwall norite, where slight positive Eu anomalies indicate the presence of cumulus plagioclase (Maier and Barnes 2003). Naldrett et al. (2009) reported elevated PGE contents in the entire Boulder Bed from a drill core intersecting much of the interval between the Merensky Reef and the UG2 unit at Rustenburg mine (Fig. 3).

While the ‘Boulder Bed’ sensu stricto is only recognised in the southern portion of the western Bushveld Complex (mainly at Impala and Rustenburg mines, with rare boulders found further east; Fig. 1), ‘boulders’ associated with

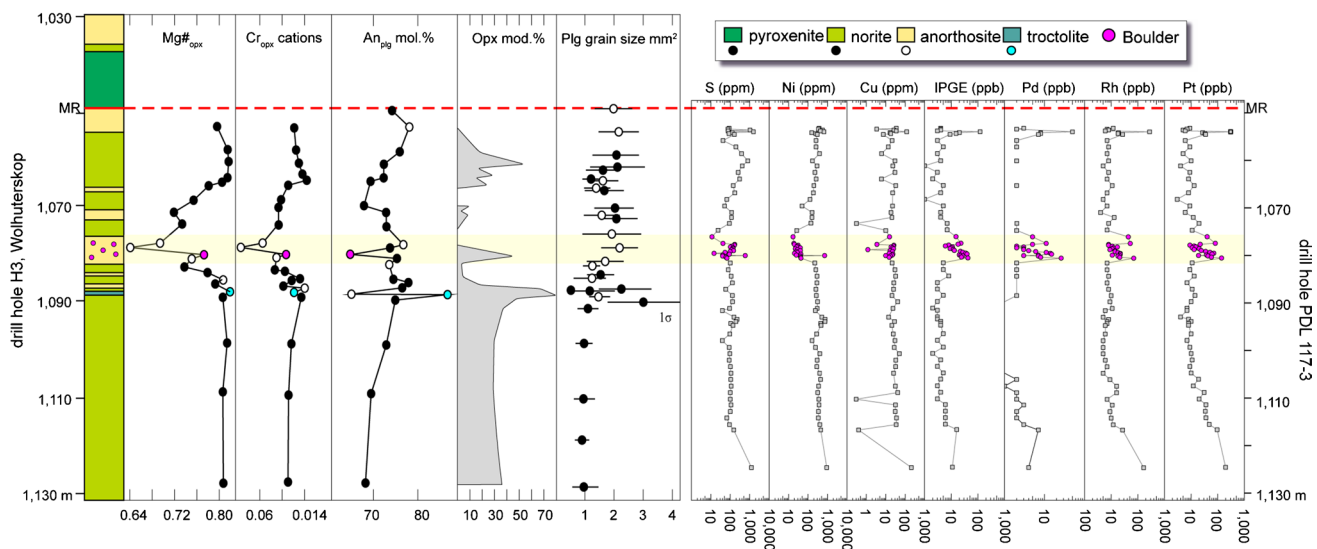


Fig. 3 Compositional and modal data from the Merensky footwall (drill hole H3, Wolhuterskop) in the western Bushveld Complex (modified from Maier and Eales 1997) combined with S and chalcophile metal contents of the Merensky footwall from Rustenburg (drill

hole PDL 117-3; Naldrett et al. 2009). Note the higher PGE concentrations and comparable S and Cu concentrations in the Boulder Bed, relative to the bracketing rock units

anorthosite have also been reported in the Bastard Reef of the northern lobe (Fig. 2D) and the hanging wall of the UG2 pyroxenite in an open pit south of Lonmin's Karee mine (Fig. 2E; Cawthorn et al. 2018). At this location, boulders occur immediately above the UG2 in a ~2-m-thick anorthosite containing dm-sized domains of mottled anorthosite. Notably, the boulders often occur along sublayer contacts in the anorthosite (Fig. 2E; Cawthorn et al. 2018).

Samples and methods

Optical microscopy and element mapping

Polished thick sections of the Boulder Bed (Table 1) were scanned and photographed in reflected light using a Leica MZ12s microscope. High-spatial resolution element maps were produced at Cardiff University using a Carl Zeiss Sigma HD analytical field emission gun scanning electron microscope (FEGSEM) equipped with two Oxford Instruments 150 mm² energy dispersive X-ray spectrometers. All X-ray element maps were produced using an accelerating voltage of 20 kV, a 120 µm final aperture in high current mode, with a nominal beam current of 8.5 nA and a dwell time of 5000–20,000 µs, at a working distance of 8.9 mm. Although the electron beam stays stable within 1% relative over periods of hours, beam current drift was optimised using a pure cobalt standard between element maps. Magnification and pixel dwell time were selected depending on the analyte (i.e. entire sections or fine-scale oscillatory zoning). An additional polished block (~10×5 cm) was mapped using a Bruker Tornado micro-XRF at CSIRO (Melbourne, Australia) at a 40 µm spatial resolution (see Barnes et al. 2020). Modal mineralogy was calculated from element maps using ImageJ™ software.

Electron backscatter diffraction (EBSD)

Electron backscatter diffraction (EBSD) is an SEM-based technique that collects data on the crystallographic orientation of any crystalline material. The studied sections were polished mechanically using a 0.3 µm suspension before being cleaned with deionised water prior to chemo-mechanically polishing with colloidal silica for 20 min. The samples were again cleaned with deionised water before being dried in air and coated with a 5-nm-thick layer of carbon using an Agar Turbo carbon coater. The EBSD analysis was performed using the Zeiss Sigma HD FEGSEM with a 20 kV beam energy and a 120 µm final aperture with the high current option activated, resulting in a nominal beam current of ~8.5 nA. The sample was mounted at 70° to the incident electron beam at a working distance of 20 mm and electron backscatter patterns were recorded using an Oxford

Instruments Nordlys EBSD detector inserted to 191 mm and AZtec version 5.0. Phases identified included anorthite and albite, augite, chromite, hypersthene, and forsterite from the American Mineralogist and HKL databases. The EBSD maps were collected with a step size of 18 µm, using 2×2 binning with an exposure time of ~60 ms with a Hough resolution of 60 and a minimum number of bands of 8. Mean angular deviations (MAD) of studied phases were below 1.0, apart from augite (1.3% modal fraction), which had a MAD of 1.06. Approximately 80.6% of pixels were indexed, with 19.4% of pixels being zero solutions.

Data processing was performed using AZtec Crystal and the open-source MTEX toolbox package (Bachmann et al. 2010). Grain reconstruction was performed using 10° thresholds on crystals greater than or equal to 10 pixels. The two-dimensional physical properties of well-constrained crystals from the host anorthosite and marginal zones were exported from AZtec Crystal and used to determine crystal size distributions (CSD). The CSDslice spreadsheet (Morgan and Jerram 2006) was used to estimate three-dimensional crystal habits, which were input into CSDcorrections software (Higgins 200) together with the plagioclase major and minor fitted ellipse length, the ellipse angle, and the grain area to produce CSD profiles. The average roundness, modal abundance, and fabric quality (or shape-preferred orientation, which is quantified by the alignment factor) were also used when producing the CSD profiles.

The crystallographic preferred orientation (CPO) of plagioclase is visualised using an orientation density function (ODF) that was calculated using a 10° halfwidth. The CPO strength is quantified by the pole figure *J*-indices (pfJ) for each axis, as well as the *J*- and *M*-indices on the orientation distribution functions (Bachmann et al. 2010; Mainprice et al. 2015). Theoretically, the pfJ and *J*-index (Bunge 1982) range from 1 (completely random) to infinity (single crystal), whereas the *M*-index (or misorientation index; Skemer et al. 2005) ranges from 0 (completely random) to 1 (single crystal). Lastly, the method of Cheadle and Gee (2017) was used to describe the three-dimensional orientation of crystals by calculating the foliation (*F*#) and lineation (*L*#) numbers. The *F*# parameter is defined as the ratio of the maximum to intermediate eigenvalues for [010] and the *L*# parameter is defined as the ratio of the maximum to intermediate eigenvalues for the [100] axes.

Electron probe microanalysis (EPMA)

Quantitative chemical analysis of plagioclase crystals was conducted at Camborne School of Mines (University of Exeter) using a JEOL JXA-8200 electron-probe microanalyser. Analyses were performed using a 30 nA electron beam accelerated to 15 kV with a beam diameter between 1 and 10 µm. Analyses were made using wavelength dispersive

Table 1 Summary of analysed sections from the Boulder Bed

Sample	Location	Method ¹	Description	Boulder mineralogy ²		Petrographic summary	Figure
				Major	Minor		
BBBC	Brakspruit, RPM	SEM-EDS, EPMA	Base of boulder	Ol, Opx, Pl	Chr, Po, Ap, Mag, Phl	Anhedral Ol, coarse-grained Chr. and fine-grained sulfides concentrated at the base of the boulder. Marginal Pl shows reverse zoning. Phl and Cl-rich Ap spatially-associated with Opx in the boulder	4
BB	Brakspruit, RPM	SEM-EDS, EPMA	Middle of boulder	Opx, Cpx, Pl	Ol, Chr, Ap, Mag, Phl	Intercumulus Pl and cumulus Opx. Coarse-grained Cl-rich Ap and Phl amongst Opx. Fine-grained Chr and sulfides disseminated throughout	4
BBTC	Brakspruit, RPM	SEM-EDS, EPMA	Top of boulder	Opx, Cpx, Pl	Chr, Ap, Mag, Phl	Subhedral Opx hosted in Pl oikocrysts with interstitial Cpx grains. Large Cl-rich Ap and Phl are associated with fine-grained sulfides. Fine-grained Chr disseminated throughout, with larger grains at the top	4
BV-BB1	Impala	μXRF	Base of boulder	Ol, Opx, Pl	Amp, Chr, Cal	Anhedral Ol and Chr concentrated at the base of the boulder. Boulder Opx shows zoning in Cr. Opx oikocrysts get richer in Cr close to the boulder	5
Bou-2	Turffontein, RPM	SEM-EDS, EPMA	Base of boulder	Ol, Opx, Pl, Amp, Chr	Cpx, Ap, Phl, Mag, Pn, Po	Pl in the margin and boulder shows reverse zoning. Clustered Chr and anhedral Ol concentrated at the base of the boulder. Ap and Amp concentrated along the margin of the boulder. Sulfides and Phl concentrated in Pl-rich portions of the boulder	6
TF-Bou	Turffontein, RPM	SEM-EDS, EBSD, EPMA	Base of boulder	Ol, Opx, Pl, Chr	Cpx, Phl, Ap, Mag, Amp, Pn, Po	Pl in the margin shows reverse zoning. Anhedral Ol and clustered Chr grains concentrated at the base of the boulder. Opx consistently rims Chr	7, 9, 11
BB-B2C	Impala	SEM-EDS, EPMA	Middle of boulder	Opx, Pl, Cpx	Ol, Chr, Ap, Phl, Mag, Qz, Po, Pn	Intercumulus Pl and Cpx in cumulus Opx. Euhedral Cl-rich Ap and coarse-grained Phl spatially-associated with Cpx. Fine-grained Chr and sulfides disseminated throughout	ESM SF2

¹ SEM-EDS, scanning electron microscopy energy dispersive spectroscopy; EPMA, electron probe micro-analyzer; EBSD, electron backscatter diffraction; μXRF, micro-x-ray fluorescence. ² Ol, olivine; Opx, orthopyroxene; Cpx, clinopyroxene; Pl, plagioclase; Chr, chromite; Mag, magnetite; Ap, apatite; Phl, phlogopite; Po, pyrrhotite; Pn, pentlandite; Ccp, chalcopyrite; Amp, amphibole; Qz, quartz; Cal, calcite

spectrometers and were calibrated to natural mineral standards supplied by P&H Developments and Astimex Scientific and quantified using the CITZAF $\phi\rho Z$ method of Armstrong (1995) implemented for JEOL. Standards analyses and results are provided in Electronic Supplementary Materials 1 and 2 (ESM 1 and 2).

Results

Petrography and element mapping

The anorthosite hosting the boulders is composed of ~92–95 mod.% cumulus plagioclase, with patches of interstitial clinopyroxene (~4–5 mod.%) and orthopyroxene (~1–4 mod.%), as well as traces of phlogopite, apatite, and quartz ($\ll 1$ mod.%; Figs. 4, 5, 6, and 7). While section thickness precludes typically transmitted light microscopy, no undulose extinction, deformation to plagioclase twin lamellae, or neoblasts were observed in our samples (ESM SF1). The petrographic observations of our sections are summarised in Table 1.

Samples BBBC-BB-BBTC These sections sample the base, middle, and top of a boulder from the Brakspruit shaft of the Rustenburg platinum mine (Fig. 4). On the scale of the whole boulder, anhedral olivine (~7–8 mod.%) is concentrated near the base, oikocrystic clinopyroxene (~10–12 mod.%) is concentrated near the top, and chromite (~0.5–1 mod.%) occurs both at the base and, to a somewhat lesser degree, along the upper margin. Orthopyroxene occurs throughout the boulder, showing an overall upward decrease in grain size from >5 mm to ~0.5–3 mm in diameter.

Relative to the bulk of the anorthosite hosting the boulder, the immediate floor rock to the boulder contains an elevated proportion of interstitial orthopyroxene (~5–10 mod.%) for ~1–2 cm as well as subordinate outer patches of clinopyroxene. Hereafter, we refer to the zone comprising intercumulus orthopyroxene (\pm olivine) as the marginal zone (bound by dashed lines in Figs. 4, 5, 6, and 7). Subhedral plagioclase (~90–95 mod.%) constitutes the remainder of the marginal zone mineralogy, together with traces of very fine-grained sulfide, chromite, and phlogopite.

Anhedral and partially serpentinised olivine (~20–25 mod.% of section BBBC) containing thin magnetite veins (~0.5 mod.%) occur at the base of the boulder where it has been partially replaced by relatively coarse-grained orthopyroxene (~50–55 mod.%). The grain size of the composite olivine-orthopyroxene crystals is <2.4 cm in diameter. Variably-sized aggregates and blocky crystals of chromite (<1–2 mm in diameter) occur amongst olivine and orthopyroxene crystals. Coarse intercumulus plagioclase (~15–20 mod.%), fine-grained

phlogopite (~0.5–1 mod.%) and very fine-grained sulfides (Po > Pn \gg Ccp; ~0.2–0.5 mod.%) generally occur within and at the margin of orthopyroxene crystals. Only traces of very fine-grained quartz, apatite, and secondary magnetite were identified.

The centre of the boulder is characterised by variably sized (0.2–1.8 mm in diameter), subhedral orthopyroxene crystals (~70–75 mod.% of section BB), with interstitial plagioclase (~10–15 mod.%). Clinopyroxene (~10–15 mod.%) sometimes occurs along the grain boundaries between plagioclase and orthopyroxene. Clinopyroxene also forms relatively large (<1.4 cm in diameter) interstitial crystals. Only very finely disseminated sulfides were identified. Magnetite (~0.6 mod.%), chlorapatite (~1–2 mod.%), and phlogopite (<1 cm in diameter, ~2–3 mod.%) rarely occur with partially uralitized clinopyroxene.

In the upper portion of the boulder, orthopyroxene (~50–55 mod.% of section BBTC) forms subhedral crystals (<1 cm in diameter). The modal abundance of oikocrystic plagioclase is comparable to that at the base of the boulder (~15–20 mod.%). Partially uralitized clinopyroxene (~20–25 mod.%) occurs as large (<1.9 mm in diameter) interstitial crystals that sometimes enclose orthopyroxene crystals. Traces of very fine-grained phlogopite and chromite are generally spatially associated with clinopyroxene. No sulfides or apatite were identified. There is only limited exposure of the upper margin of the boulder, which is relatively sharp, displaying a cluster of several blocky chromite crystals.

Sample BV-BB1 This sample is from the base of a boulder from Impala mine and was mapped using micro-XRF (Fig. 5). The base of the boulder is partially circumscribed by a zone of pure plagioclase (~5 mm wide) as well as plagioclase-rich zones with intercumulus pyroxenes. Moreover, the size and abundance of intercumulus pyroxene gradually decrease with distance from the boulder. Anhedral olivine (<1 cm in diameter) is concentrated near the base of the boulder. It shows irregular, strongly rounded morphologies and is enclosed within coarse-grained orthopyroxene. The olivine is partially replaced by secondary magnetite. Coarse-grained orthopyroxene and interstitial plagioclase comprise the bulk of the boulder in this sample. Medium-grained chromite occurs at the base of the boulder, notably around the margins of olivine, whereas finer-grained chromite crystals are observed within the boulder (Fig. 5). Traces of calcite and amphibole were also identified.

Samples Bou-2 and TF-Bou These sections sample the bases of boulders from the Turffontein section of Rustenburg Platinum Mine (Figs. 6 and 7). Their marginal zones comprise cumulus plagioclase (~75–85 mod.%) and intercumulus orthopyroxene (~10–15 mod.%). Directly below the

Fig. 4 A PPL scans of sections BBBC, BB, and BBTC, which sample the base, middle, and top of a boulder, respectively. **B** Mg–Ca–Cr–log[K] SEM–EDS element map. **C** Si–log[K]–P–S–Fe SEM–EDS element map. Dashed lines outline the marginal zone (i.e. the extent of intercumulus orthopyroxene) and red arrows represent EPMA transects (see Fig. 8; ESM 1). Abbreviations: ol, olivine; cpx, clinopyroxene; opx, orthopyroxene; pl, plagioclase; chr, chromite; sul, sulfides; ap, apatite; phl, phlogopite; mag, magnetite

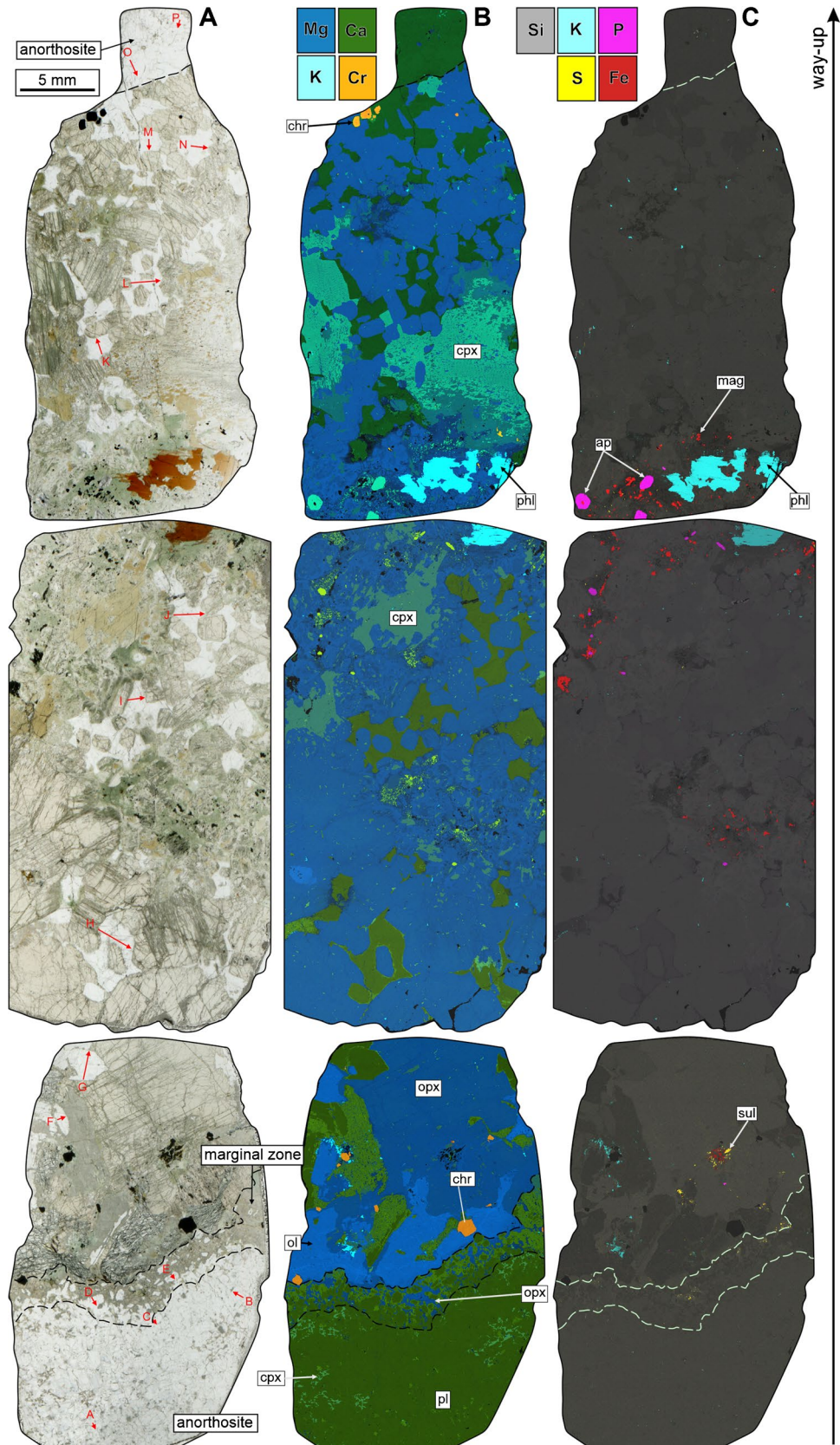
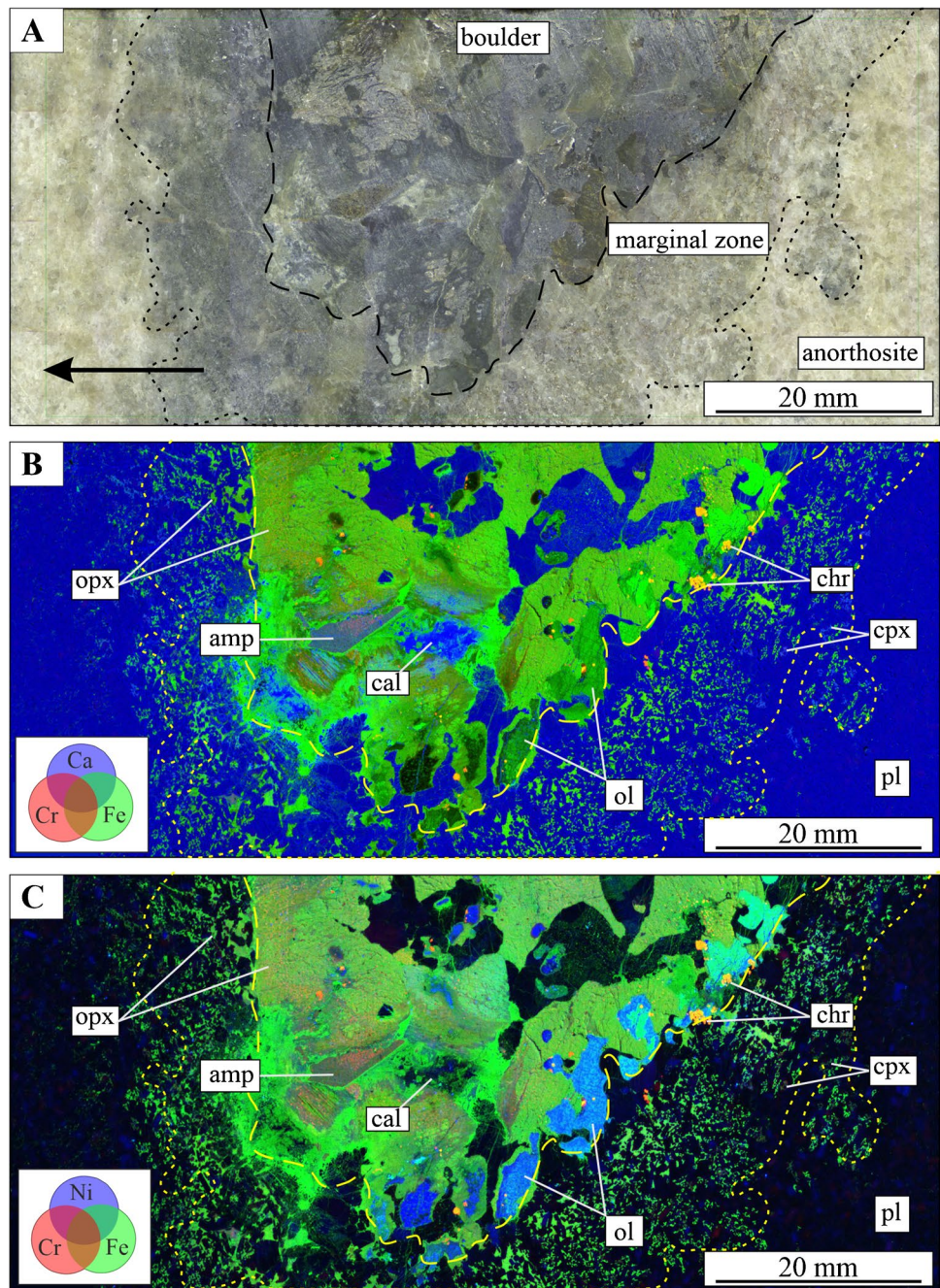


Fig. 5 **A** Photograph of sample BV-BB1 showing a pyroxenitic boulder and its marginal zone. **B** Cr-Fe-Ca XRF map of sample BV-BB1. **C** Cr-Fe-Ni XRF map of sample BV-BB1. Abbreviations: ol, olivine; opx, orthopyroxene; plg, plagioclase; chr, chromite; amp, amphibole; cal, calcite

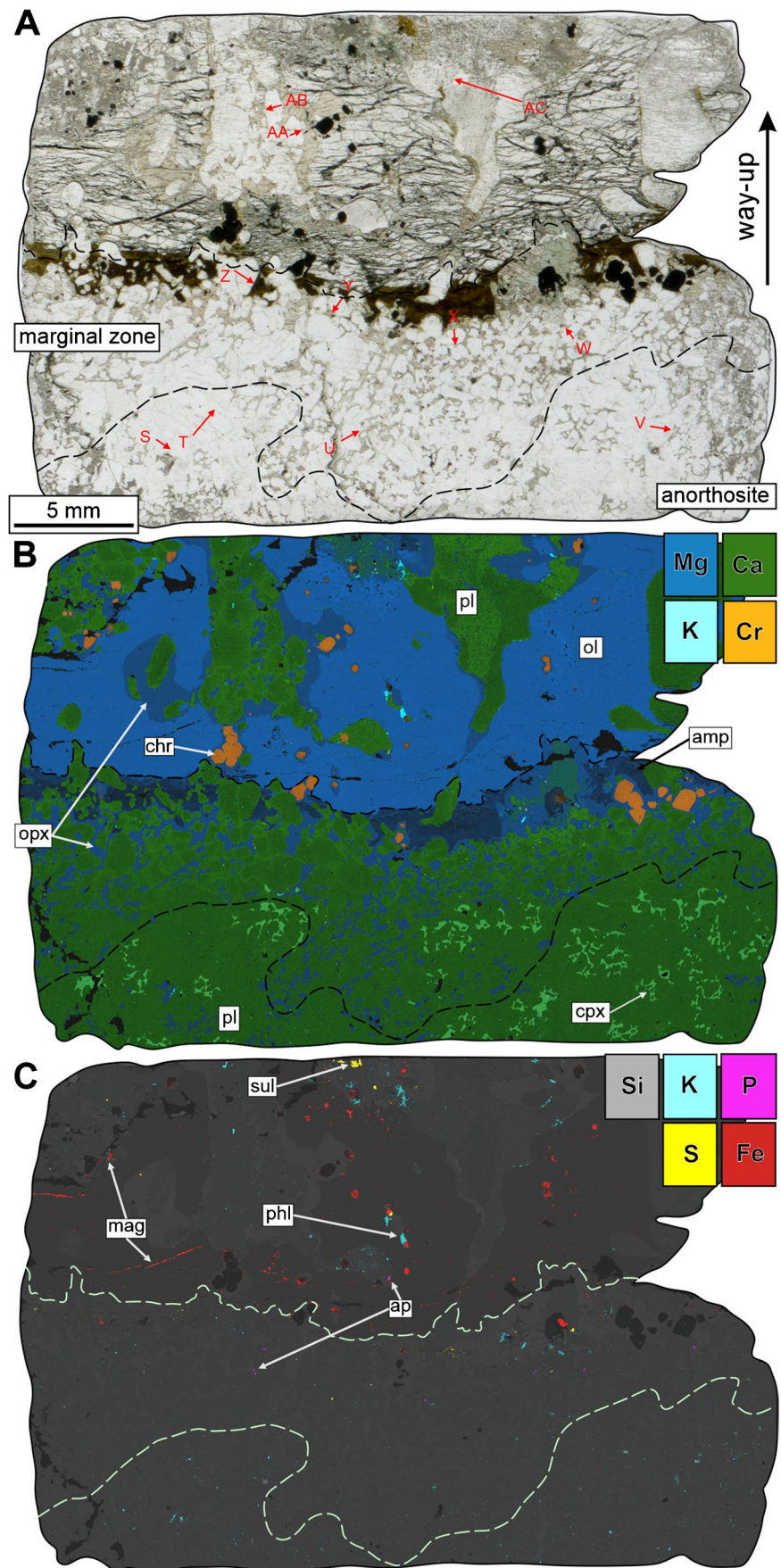


marginal zones, clinopyroxene (~3–5 mod.%) becomes the dominant intercumulus phase. Traces of fine- to medium-grained amphibole and chromite occur at the margins of intercumulus orthopyroxene. Chromite crystals sometimes form clusters of ≥ 2 crystals (~3–5 mod.%).

The basal portions of the boulders comprise relatively coarse-grained and partially serpentinised (<3 mm in diameter; ~40–50 mod.%) olivine that is partially rimmed by orthopyroxene (~10–35 mod.%). The base of sample

Bou-2 (Fig. 6) is lined by a ~0.2 cm rim of amphibole (~10 mod.%), together with traces of very fine-grained mica, sulfide, and apatite—this is not observed in sample TF-Bou (Fig. 7). The marginal zones consist of fine- to medium-grained cumulus plagioclase crystals amongst intercumulus orthopyroxene (\pm olivine \pm amphibole) that is sometimes spatially associated with clusters of blocky chromite crystals. (Figs. 6B and 7B). Fine-grained phlogopite and sulfides (Po > Pn and no Ccp; <0.5 mod.%) occur at the margins of olivine-orthopyroxene crystals (within plagioclase-rich

Fig. 6 **A** PPL scan of section Bou-2, which samples the base of a boulder. **B** Mg–Ca–Cr–log[K] SEM–EDS element map. **C** Si–log[K]–P–S–Fe SEM–EDS element map. Dashed lines outline the marginal zone (i.e. the extent of intercumulus orthopyroxene) and red arrows represent EPMA transects (see Fig. 8; ESM 1). Abbreviations: ol, olivine; cpx, clinopyroxene; opx, orthopyroxene; pl, plagioclase; chr, chromite; sul, sulfides; ap, apatite; phl, phlogopite; amp, amphiboles; mag, magnetite



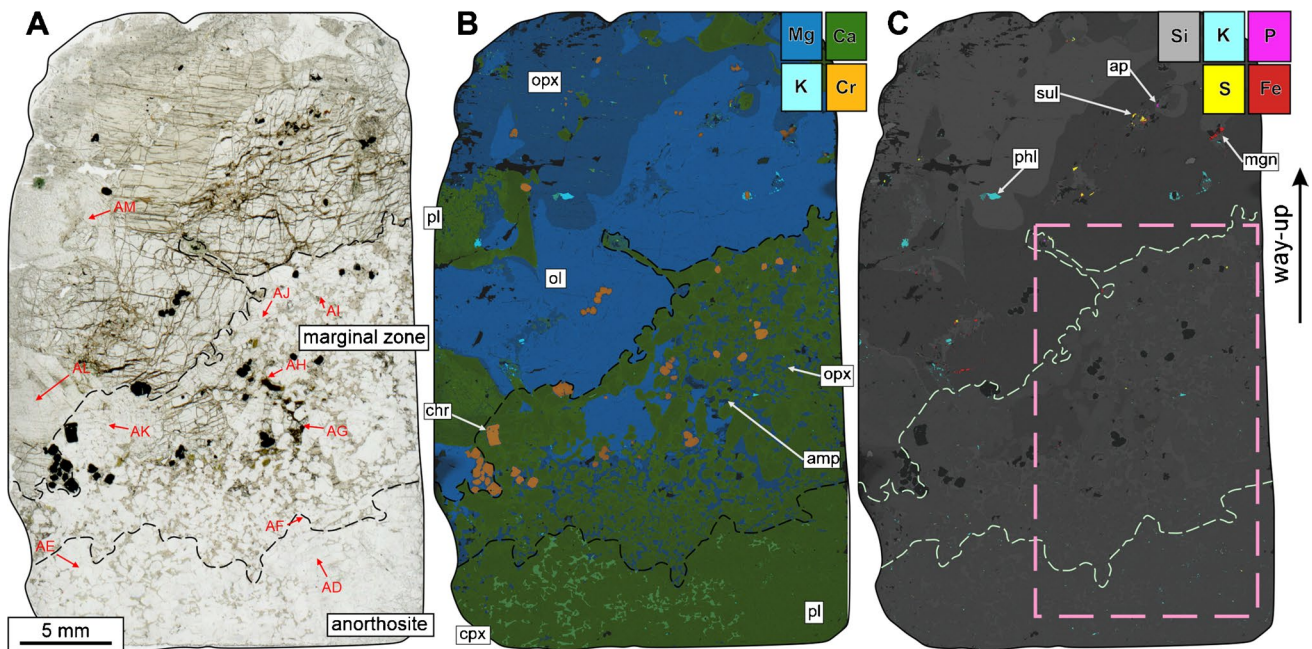


Fig. 7 **A** PPL scan of section TF-Bou, which samples the base of a boulder. **B** Mg–Ca–Cr–log[K] SEM–EDS element map. **C** Si–log[K]–P–S–Fe SEM–EDS element map. Dashed lines outline the marginal zone (i.e. the extent of intercumulus orthopyroxene) and red arrows represent EPMA transects (see Fig. 8; ESM 1). Abbreviations: ol, olivine; cpx, clinopyroxene; opx, orthopyroxene; pl, plagioclase; chr, chromite; ap, apatite; phl, phlogopite; amp, amphiboles; sul, sulfides; mag, magnetite

domains), yet sulfides and phlogopite are not spatially associated.

Sample BB-B2C This section samples the middle of a boulder from the Impala mine (Sup. Figure 2). The section has several similarities with the lower-central portion of the boulder from the Brakspruit section (Fig. 4), including (1) the grain sizes of plagioclase and orthopyroxene decrease upward through the boulder; (2) olivine that is partially rimmed by orthopyroxene occurs towards the base; (3) the mode of uralitized clinopyroxene increases upward through the boulder; (4) fine-grained magnetite is spatially associated with clinopyroxene; (5) interstitial phlogopite and Cl-rich apatite are spatially associated with each other; (6) only very fine-grained sulfides are present.

Plagioclase composition

Cumulus plagioclase in the host anorthosite Six plagioclase crystals from the underlying anorthosite (samples BBBC, Bou-2, and TF-Bou) and two crystals from the overlying anorthosite (sample BBTC; Fig. 8A; ESM 1) were chemically analysed rim to rim. The crystals are ≤ 1 –2 mm in diameter and possess An contents mostly ranging from ~ 80 to 75 mol.% with seemingly no systematic variation

indicative of compositional zoning. There is, however, one exception (transect AE in Fig. 7) occurring just beneath the marginal zone, where the outer ~ 0.2 mm is ~ 8 mol.% more anorthitic than the corresponding transect centre.

Cumulus plagioclase in the marginal zone Fifteen crystals present in the marginal zones were analysed (Fig. 8B; ESM 1). The crystals have broadly similar morphologies as those in the host anorthosite (~ 1 –2 mm in diameter and subhedral), yet those present in the marginal zones record subtle to strong reverse zoning, where the outermost analyses can be up to 15 mol.% more anorthitic than the corresponding central analyses. The centres of crystal transects have An contents of ~ 83 –76 mol.% and the corresponding transect margins (i.e. the outer 0.5–0.3 mm) have An contents of ~ 88 –95 mol.%.

Plagioclase within boulders Fifteen crystals present within the defined outline of the boulders were analysed (Fig. 8C; ESM 1). This includes: (i) two cumulus grains (Fig. 6); (ii) seven intercumulus grains from the lower portions of boulders (Figs. 4, 6, and 7; ESM Fig. S2); (iii) six intercumulus grains from the upper portions of boulders (Fig. 4). The two cumulus grains in section Bou-2 (AA and AB; Fig. 6) are the smallest (< 1 mm in diameter) and show pronounced reverse

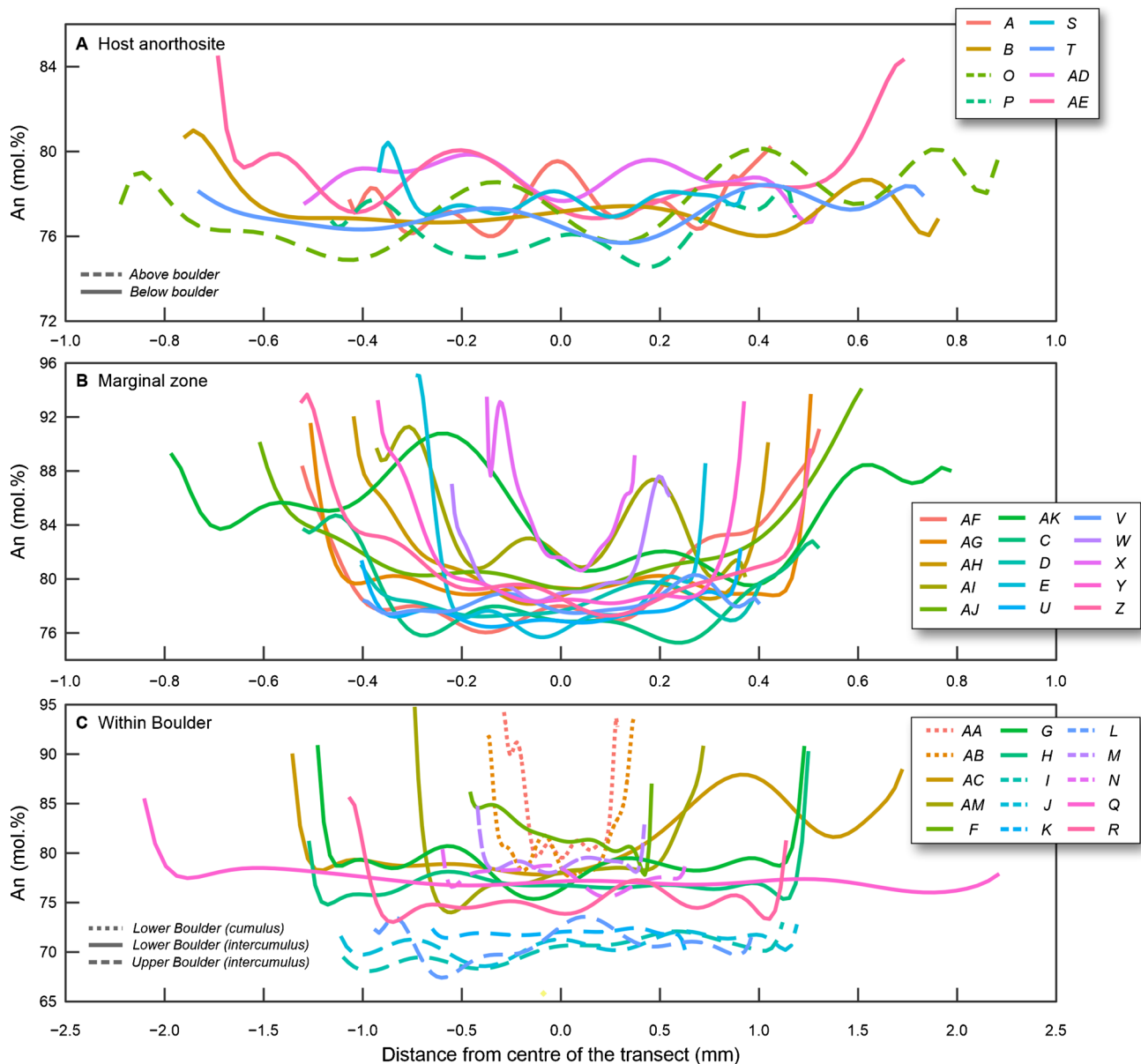


Fig. 8 Rim-core-rim EPMA transects of plagioclase crystals measured in the host anorthosite (A), marginal zone (B), and within boulders (C). The profiles have been smoothed by polynomial approxima-

tion. The corresponding EPMA transects are annotated in Figs. 4, 6, and 7, and ESM Fig. S2 as well as reported in ESM 1

zoning comparable to crystals sampled in the marginal zone (i.e. An contents of transect edges are > 10 mol.% greater than corresponding centres). Intercumulus plagioclase crystals sampled from the lower halves of boulders have relatively constant An contents (~78–74 mol.%), yet with an outer ~0.1–0.2 mm that is up to 10 mol.% more anorthitic. In contrast, intercumulus plagioclase sampled from the upper halves of boulders has markedly lower constant An contents (~71–67 mol.%) with no clear systematic variation. However, two exceptions to this (transects M and N; Fig. 4) have

An contents of ~78–79 mol.% with slightly more anorthitic rims; these grains occur amongst the chromite-bearing upper surface of a boulder.

Microstructural analysis of plagioclase crystals

Plagioclase crystals from the host anorthosite and marginal zone of section TF-Bou (Fig. 7) were analysed by EBSD (Figs. 9, 10, and 11). The physical characteristics of plagioclase crystals are illustrated in Fig. 9A, B, and C,

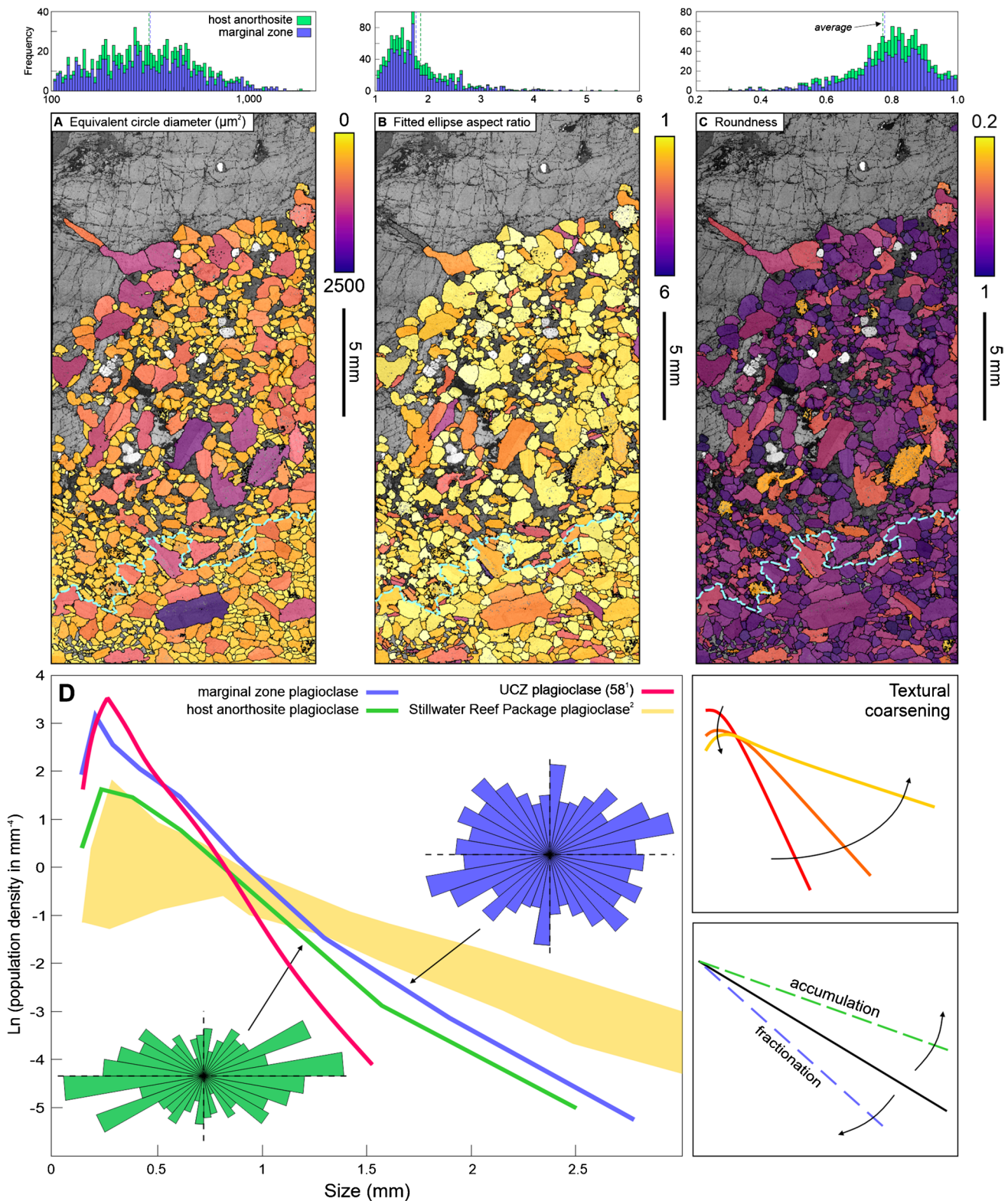


Fig. 9 Physical characteristics of plagioclase crystals at the base of a boulder in section TF-Bou (Fig. 7; Tab. 2). A–C Maps and stacked histograms of equivalent circle diameter (ECD; **A**), aspect ratio (**B**), and roundness (**C**) exported from AZtec Crystal software. **D** Plagioclase CSD plot and rose diagrams exported from CSDcorrections

(Higgins 2002). Underlain are CSD profiles of plagioclase crystals from the Upper Critical Zone (Fig. 11 and sample 58 from Boorman et al. 2004¹) and from the JM reef package of the Stillwater Complex (Jenkins et al. 2022²). Additional plots display theoretical CSD profiles (Marsh 1988; Higgins 2002; Boorman et al. 2004)

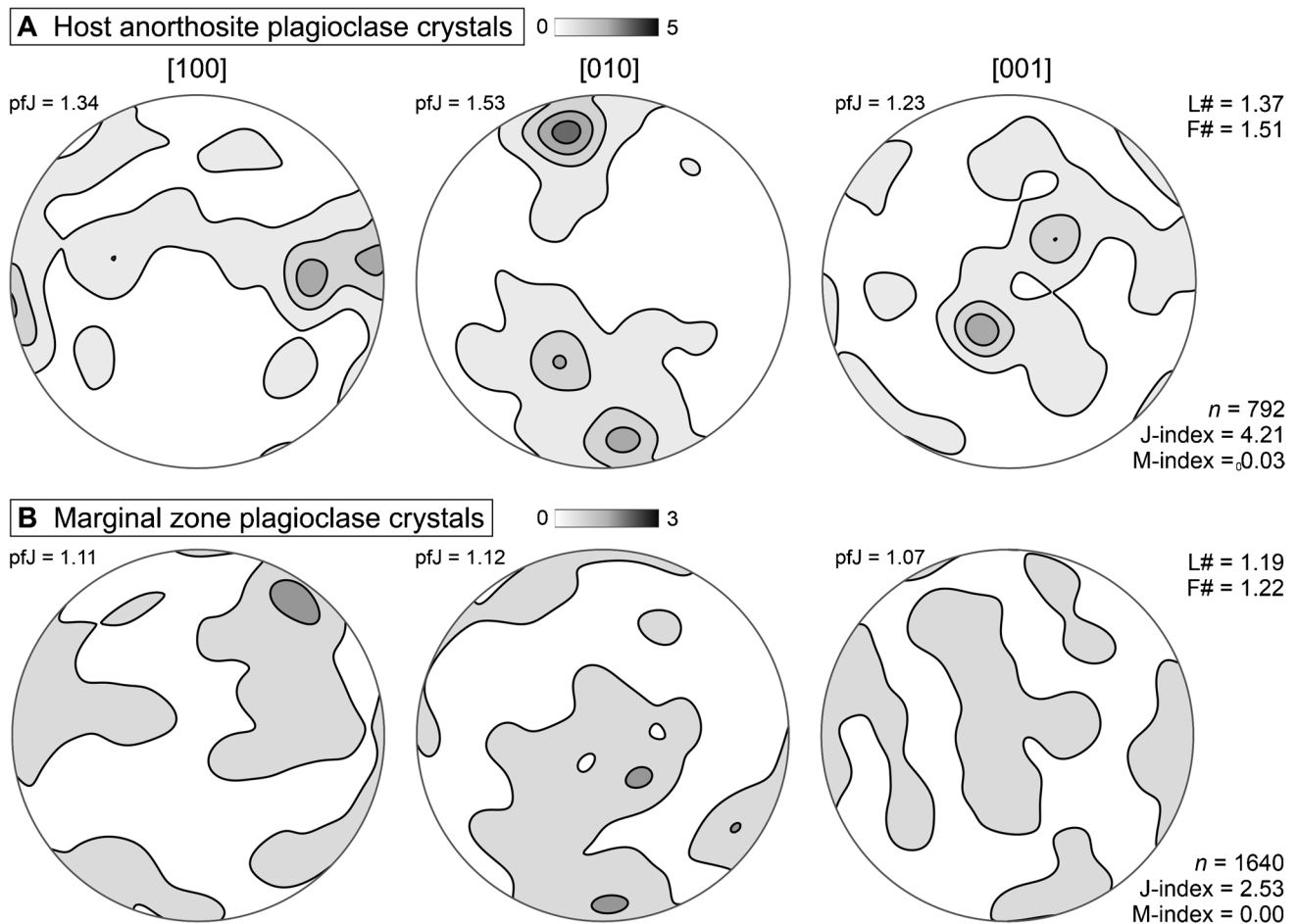


Fig. 10 Lower hemisphere, equal-area pole figures of the [100], [010], and [001] axes of plagioclase crystals in the host anorthosite (A) and marginal zone (B). The pfJ, M-index, and J-index values

together with the L# ($[100]e_1/e_2$) and F# ($[010]e_1/e_2$) are given for each grain group (see Electron backscatter diffraction (EBSD) section)

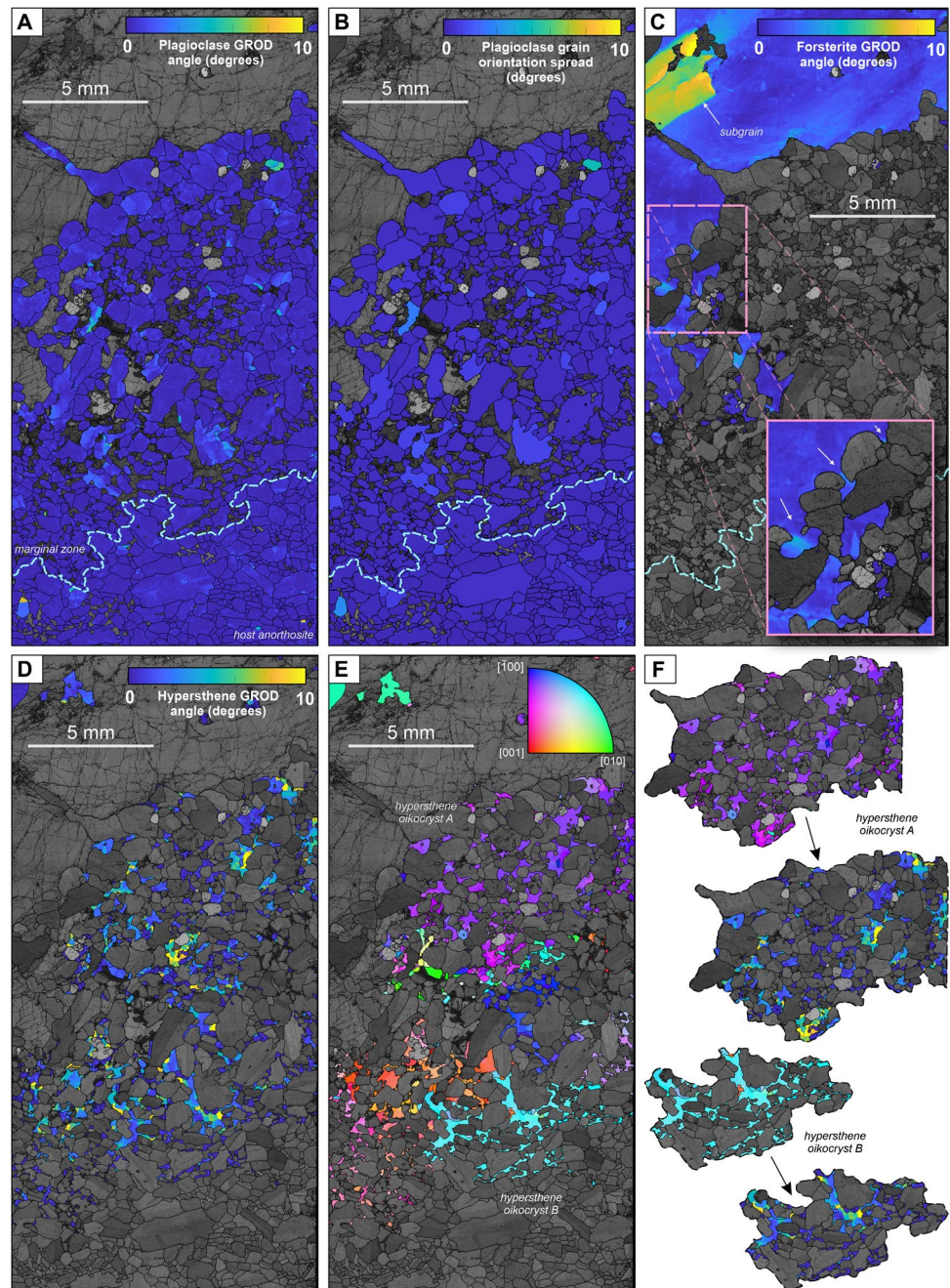
summarised in Table 2 and fully reported in ESM 3. These data show that crystals in the host anorthosite and marginal zone have near-identical physical properties (Table 2).

The crystal size distribution (CSD) of plagioclase crystals was determined using the CSDcorrections software (Higgins 2002), and the crystal shape was determined using CSDslice (see Table 2; Morgan and Jerram 2006). The CSD patterns of plagioclase crystals in the host anorthosite and marginal zone have similar profiles in that they display convex-up patterns in crystals ranging from ~0.2 to 0.5 mm and broadly flat to shallow concave-up patterns for crystals > 0.4 mm (Fig. 9D). Our CSD profiles are shallower than those recorded by Upper Critical Zone crystals sampled from the Jagdlust section of the eastern lobe of the Bushveld Complex (Boorman et al. 2004; Fig. 9D), but are steeper, with less-defined convex-up patterns at smaller crystal sizes, than those from the JM reef package rocks of the Stillwater Complex (Jenkins et al. 2022).

Rose diagrams were also produced using CSDcorrections, which show that the plagioclase crystals are generally aligned parallel to rock layering in the critical zone and thus, parallel with the long axes of boulders (Jones 1976). The strength of the mineral alignment (i.e. shape preferred orientation; SPO) is quantified using the alignment factor, whereby a value of 1 represents perfect alignment and a value of 0 represents perfectly random orientation (see Holness et al. 2020). Plagioclase in the host anorthosite has an alignment factor of 0.28, and those in the marginal zone have an alignment factor of 0.11 (Table 2).

Electron backscatter diffraction analysis was conducted at the base of the boulder TF-Bou (Fig. 7). Our aim was to identify potential evidence for viscous deformation (such as dislocation creep or diffusion-controlled processes such as dissolution-reprecipitation; Holness et al. 2017; Vukmanovic et al. 2019) in cumulus plagioclase crystals that host the boulders. Typically, magmatic samples that have undergone

Fig. 11 **A** Grain reference orientation deviation (GROD) angle maps of plagioclase, whereby pixels within a given grain are coloured by the difference in orientation angle relative to the grain average. **B** Grain orientation spread (GOS) map of plagioclase. Grains are coloured by the average misorientation angle of each pixel within a given grain relative to the average orientation of the same grain. **C** GROD angle map of forsterite. Note the subgrain in the upper left as well as the downward percolative textures of olivine into cumulus plagioclase of the host anorthosite. **D** GROD angle map of hypersthene. Note the high degrees of misorientation as indicated by the yellow colours. **E** Mean orientation map of hypersthene where similar colours indicate similar orientations for the grains. One can observe regions where hypersthene crystals preserve similar orientations, which suggests that they are oikocrysts, which suggests that they are oikocrysts. **F** Enhanced view of internal misorientation within two hypersthene oikocrysts. Note that the internal misorientation is relative to each exposed portion of the oikocryst itself



significant viscous deformation through compaction have a fabric defined either by crystal shapes or preferred orientations (Holness et al. 2017). Features such as dislocation creep (as evidenced by undulose extinction or mechanical twins) and dissolution-precipitation (as evidenced by truncation of crystals, the interpenetration of crystals, or suture contacts) may also be expected.

Figure 10 represents equal-area, lower hemisphere pole figures of the [100], [010], and [001] axes distribution for plagioclase crystals in the host anorthosite and marginal

zone. Because of the ubiquitous presence of twins in the plagioclase crystals, we calculated the orientation distribution function (ODF) using every measurement available, using a 10° halfwidth for the calculation. The pole figures display the orientation of the crystallographic axis of plagioclase crystals in three dimensions, where the strength of axis distribution is quantitatively assessed using the p_fJ , J -, and M -indices (Table 2) and their relative symmetry is reported using the $F\#$ and $L\#$ values (Methods section; Fig. 10; ESM 4). If the crystallographic axes are distributed in a way that

Table 2 Summary of the physical properties and fabric indices of plagioclase crystals from the host anorthosite and marginal zone of the Boulder Bed

Group	Count	Mode (%)	¹ ECD (μm^2)		Aspect ratio		Roundness		CSDslice shapes			Mean orien. (°)	Alignment factor (AF)	J-index	M-index
			\bar{x}	$I\sigma$	\bar{x}	$I\sigma$	\bar{x}	$I\sigma$	Short	Medium	Long				
All crystals	1093	58.8	380.6	253.1	1.77	0.63	0.760	0.113	1.0	1.3	1.9	0.898	0.16	2.75	0.01
Host anorthosite	344	17.2	372.5	235.1	1.85	0.65	0.758	0.190	1.0	1.4	2.0	0.840	0.28	4.21	0.03
Marginal zone	749	41.6	384.4	261.0	1.76	0.61	0.761	0.114	1.0	1.4	1.8	0.907	0.11	2.53	0.00

¹Well-defined grains with equivalent circle diameters (ECD) of $>100 \mu\text{m}^2$ were considered. ²J- and M-index values were computed using the orientation distribution function (ODF) of all measurements of anorthite

is non-random, the subject phase has a crystallographic preferred orientation (CPO). A non-random distribution may manifest as a point maximum if the axes are clustered along a specific direction or as a girdle if the axes are randomly distributed along a plane.

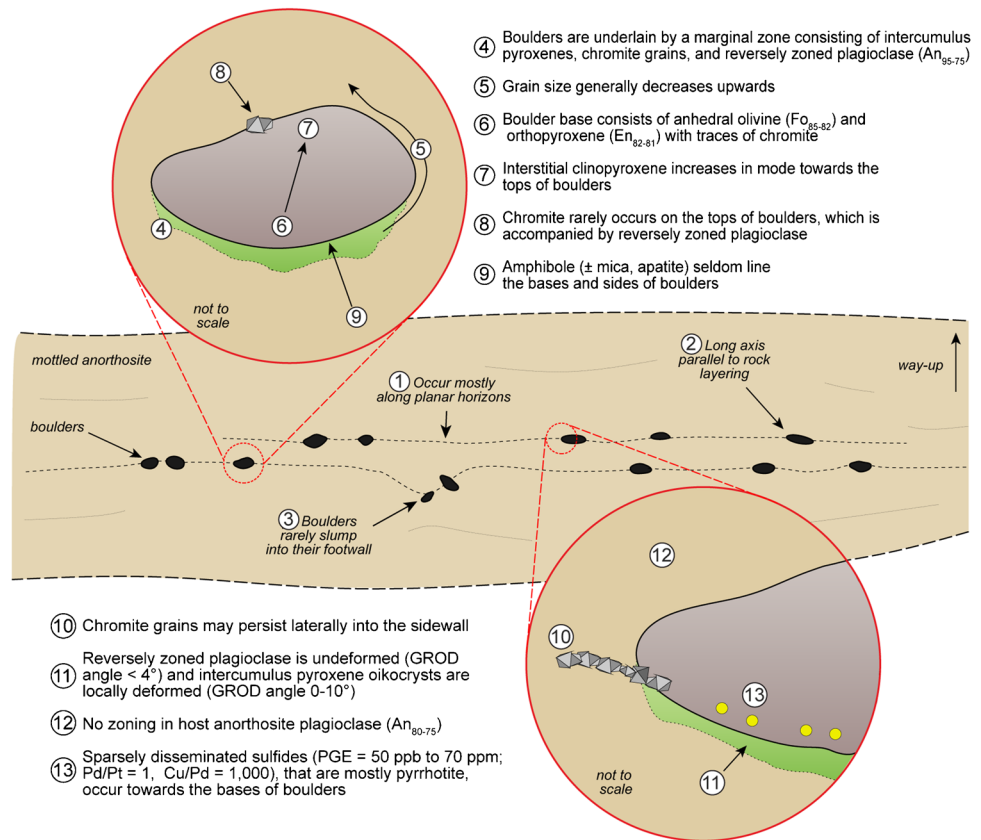
Pole figures of plagioclase crystals in the host anorthosite (Fig. 10A) show a cluster of [010] axes, i.e. a direction that is perpendicular to the bedding plane of the host rock. The [100] axes are found to cluster on the bedding plane. While the fabric strength is low (AF=0.28; J-index=4.21; M-index=0.03), our data indicate a non-random orientation of plagioclase in the host anorthosite, one that is comparable to B-type axis fabrics that are known to develop in tabular cumulus minerals of layered intrusions (Cheadle and Gee 2017; Holness et al. 2017). Conversely, pole figures of plagioclase crystals in the marginal zone show no clearly defined CPO (Fig. 10B), as indicated by their relatively weaker fabric indices (AF=0.11; J-index=2.53; M-index=0.00).

Figure 11A is a map of the grain reference orientation deviation (GROD) angle, which reports the angular deviation of each pixel within a given grain relative to the mean orientation of the same grain. Figure 11B is a grain orientation spread (GOS) map of plagioclase, where individual grains are coloured by the average of misorientation angles recorded within each pixel of a given grain relative to the average orientation of the same grain. In GROD and GOS maps, higher values (Fig. 11) correspond to higher degrees of intragranular deformation (Brewer et al. 2009; Allain-Bonasso et al. 2012). Plagioclase in both the host anorthosite and marginal zone display negligible degrees of misorientation, inconsistent with significant plastic deformation (Brewer et al. 2009). This determination is further supported by the absence of neoblasts and the preservation of magmatic twins. Only localised misorientation is seemingly randomly distributed throughout plagioclase crystals of the marginal zone.

Microstructural analysis of ferromagnesian crystals

Hypersthene, augite, and forsterite were also indexed during the acquisition of EBSD data. While there are too few of these crystals to illustrate and quantify meaningful fabric data, misorientation within these crystals can still be visualised. Figure 11C is a GROD angle map of forsterite, where while a subgrain is present in the upper left portion of the map, no systematic intra-crystalline deformation is present. Furthermore, the textural relationship olivine shares with cumulus plagioclase indicate that it crystallised after plagioclase. Figures 11D, E, and F illustrate GROD angle and grain maps for hypersthene. Hypersthene oikocrysts in the marginal zone display variable degrees of intra-crystalline misorientation, possibly consistent with a limited degree of plastic deformation. Our data illustrates that the hypersthene

Fig. 12 Schematic diagram summarising the key features of the Boulder Bed



present in the marginal zone, as well as augite present in the host anorthosite, crystallised after plagioclase and that no further episode of deformation, plastic or magmatic, occurred after that.

Discussion

Previous models for the formation of the Boulder Bed

The origin of the Boulder Bed has remained controversial due to its highly unusual features, which are summarised in Fig. 12. A number of contrasting petrogenetic models addressing the formation of the Boulder Bed have been proposed.

(i) In situ models advocate the crystallisation of pyroxene and plagioclase from residual melt trapped in a relatively impermeable anorthosite matte (Ferguson and Botha 1963; Vermaak 1976; Lee and Sharpe 1980). The model could explain the spherical shape and ‘up-right’ crystal sequence of the boulders as well as the occurrence of amphibole (and mica) in some boulders relative to the remainder of the Critical Zone. However, the model is inconsistent with the lateral alignment of boulders, an

abundance of relatively unevolved olivine, orthopyroxene, and plagioclase, the presence of chromite, and the negligible proportions of quartz in the boulders. A model of essentially in situ fractionation also has difficulty accounting for the high PGE concentrations (including the relatively immobile IPGE) of boulders relative to the host anorthosite (Fig. 3; Maier and Barnes 2003; Naldrett et al. 2009).

(ii) Ex situ models include the sinking of boulders formed from magma ‘fingers’ generated during the influx of new magma (Campbell et al. 1983) and the sinking of fragments of a structurally-disrupted pyroxenitic layer (Jones 1976), which may originally have formed part of the Merensky Reef or correlate to the Pseudoreefs of the northern portion of the western Bushveld lobe (Jones 1976; Maier and Eales 1997). The latter model can explain the relatively unevolved composition of the main rock-forming minerals, the PGE enrichments in some boulders, and the fact that boulders and the Pseudoreefs never occur at the same locality. However, the break-up of a ‘Merensky Reef’ or Pseudoreef would be expected to result in fragments of variable size, shape, and orientation, and chromite would not be expected to line the surfaces of boulders. More importantly, the model cannot explain the occurrence of boulders in anorthosite overlying the UG2 pyroxenite (Fig. 2E).

(iii) Maier and Barnes (2003) proposed a modification of the ex situ model whereby a broken-up pyroxenite layer and its noritic host were modified by late-magmatic reactive porous flow involving an ascending Si-undersaturated volatile phase. This model could explain the association of unevolved pyroxene, olivine and plagioclase with amphibole, the lack of quartz, the chromite selvages, the reversely zoned plagioclase and the presence of anorthositic bleach zones around some of the boulders, and the formation of the anorthosite layer hosting the boulders. However, as in the case of other ex situ models (e.g. Jones 1976), the relatively uniform size and shape of the boulders remain enigmatic.

(iv) Maier (1995) and Maier et al. (2021) described ‘microboulders’ or ‘mottles’ in the upper critical zone sampled at the Wildebeestfontein North Section at Impala Platinum Mines. The mottles contain anhedral olivine rimmed by intercumulus orthopyroxene and surrounded by a halo of strongly reverse-zoned plagioclase and phlogopite. They proposed that these features formed in response to a proto-norite being fluxed by acidic fluids migrating along layer contacts. The fluids triggered the incongruent dissolution of pyroxenes as well as the leaching of alkalis from plagioclase to form a calcic anorthositic restite of reversely zoned plagioclase. Secondary olivine and pyroxene were locally precipitated in fluid channels where mixing occurred between relatively cold Si-undersaturated and hot Si-saturated fluids.

Towards an internally consistent petrogenetic model

The data presented in this study suggest that the Boulder Bed formed through both primary magmatic and secondary hydromagmatic processes. We distinguish the following petrogenetic stages:

Disintegration of proto-cumulates We hypothesise that a (leuco)noritic cumulate pile, representing the temporary chamber floor, was overlain by sulfide-bearing pyroxenitic cumulates upon chamber replenishment following Nicholson and Mathez (1991; Fig. 13A). The heat from the replenishment event triggered partial melting of the (leuco)norite, generating an anorthosite restite and a reaction front between the ultramafic cumulates and upwelling partial melts (Fig. 13B, C), as suggested previously at the Basis-toppen Sill (Naslund 1986), Rum (O’Driscoll et al. 2009), and the Bushveld Complex (Eales et al. 1986; Scoon and Mitchell 2012; Scoon and Costin 2018). This process could explain the relatively thicker marginal zone at the bases of boulders (this study; Fig. 4), the precipitation of chromite by Cr_2O_3 liberated from the partially molten anorthosite (Scoon and Costin 2018; Figs. 4, 6, and 7), and the occurrence of unevolved anhedral olivine via incongruent dissolution of orthopyroxene (Shaw and Dingwell 2008; Maier et al. 2021; Marsh et al. 2021; Figs. 4, 5, 6, and 7). If the replenishing magma intrudes the noritic cumulates as a sill (e.g. Mungall

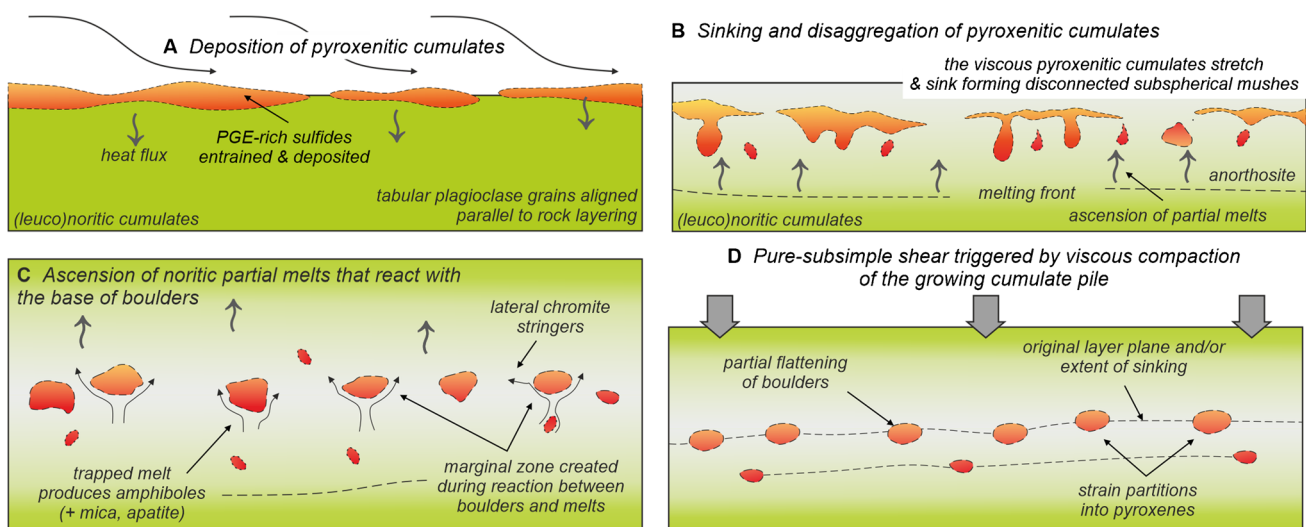


Fig. 13 **A** Deposition of pyroxenitic cumulates atop (leuco)noritic cumulates during magma chamber replenishment. **B** The influx of heat triggers partial melting of the (leuco)noritic floor rocks, which facilitates the disaggregation and sinking of the pyroxenitic cumulates. **C** The upwelling (leuco)noritic partial melts react with the bases of boulders further promoting their disaggregation and rounding. This reaction causes: (i) incongruent dissolution of orthopyroxene to form unevolved anhedral olivine; (ii) coarsening of the boulder

bases; (iii) plagioclase resorption and generation of reverse zoning; (iv) dissolution of base metal sulfides; (v) precipitation of chromite along the base and sides of boulders; and (vi) the precipitation of amphibole and other late-stage silicates in some cases. The upwelling of melts also explains the lack of comparable features on the upper margin of boulders. **D** Late-stage viscous compaction causes partial flattening of boulders and intra-crystalline deformation of intercumulus pyroxenes

et al. 2016), and both the noritic floor and roof rocks may partially melt to form bracketing anorthosite. In either case, the pyroxenitic cumulates could sink and dismember prior to complete solidification to form fragments within the feldspathic mush that would later become boulders. Alternatively, fluxing of volatiles from cooler rocks at deeper levels of the cumulates could have triggered the partial dissolution of noritic proto-cumulates to form anorthosite (Meurer et al. 1997; Maier et al. 2021).

Deformation of boulders and bracketing anorthosite The hypothetically partially molten and (or) dissolved pyroxenite layer was rheologically weakened and underwent hot subsimple shearing triggered by the sliding of hanging-wall rocks towards the centre of the progressively subsiding intrusion (Maier et al. 2013; Vukmanovic et al. 2019). While there is evidence for localised macroscopic deformation (Fig. 2C), crystal-scale deformation was only recorded within intercumulus pyroxenes of the marginal zone (Fig. 11). We interpret this as a result of strain partitioning during late-magmatic pure to subsimple shear in response to viscous compaction of the cumulate pile (Fig. 13D), whereby strain was accommodated within the less-component melt generated during the reaction between the boulders and (leuco)noritic partial melt (Vigneresse and Tikoff 1999). This process can explain the weakly flattened appearance of boulders (Fig. 2E; Holness et al. 2017). If some form of shearing had occurred, one might expect to see evidence for dynamic recrystallisation (e.g. bent twins, undulose extinction, sub-grains, serrated or lobate grain boundaries; Holness et al. 2017) recorded in bracketing cumulus plagioclase. Vukmanovic et al. (2019) and Maier et al. (2021) reported microtextural evidence for the dynamic crystallisation of cumulus plagioclase within upper and critical zone anorthosites, respectively, and ascribed these features to slumping and subsidence of crystal mush. However, no such features were consistently observed in our samples (Fig. 11; ESM Fig. S1). One could argue that static annealing of cumulus plagioclase under super-solidus conditions (> 500 °C) diluted or overprinted evidence for internal strain and CPO while preserving any SPO (Hunter 1996; Heilbronner and Tullis 2002; Piazzolo et al. 2006; Holness et al. 2017). The degree of static annealing is likely to increase with intrusion size and depth (Holness et al. 2017), and given the size of the Bushveld Complex (Smith and Maier 2021) and the prolonged cooling history of the cumulates (~20–80 kyear; Cawthorn and Walraven 1998), super-solidus conditions could have been sustained. However, static recrystallisation would eradicate the observed reverse zoning (Holness et al. 2017; Robb and Mungall 2020), unless reverse zoning of plagioclase formed after grain annealing. Further microstructural and along-plane investigations are required to understand how these

processes gave rise to planar layers of seemingly isolated boulders of comparable size and composition.

Reverse zoning of plagioclase Several studies report the reverse zoning of cumulus plagioclase in upper critical zone anorthosite (Maier and Eales 1997; Robb and Mungall 2020; Smith et al. 2021; Maier et al. 2021). In this study, cumulus plagioclase within the host anorthosite contains no systematic compositional zoning, whereas cumulus plagioclase within the marginal zone becomes increasingly reversely zoned with proximity to the boulder bases (i.e. increasing in intensity with increasing volumes of intercumulus pyroxenes; Figs. 8 and 12). Reverse zoning of plagioclase may arise from dissolution-reprecipitation (Humphreys 2009; Bennett et al. 2019) or the preferential leaching of Si and Na by Si-undersaturated fluids and (or) melts (Baker and Boudreau 2019; Maier et al. 2021; Marsh et al. 2021). In the absence of core-rim microtextural evidence and the presence of relatively disrupted plagioclase grains (e.g. lower textural indices) with highly anorthitic rims in the marginal zone, we favour Ca-rich rim formation by the preferential removal of alkalis during interaction with residual (leuco)noritic partial melt, which coincided with the precipitation of olivine and spinel at the base of boulders. A late-magmatic origin for plagioclase reverse zoning is also preferred since, under prolonged super-solidus conditions, reverse zoning may not be preserved (Robb and Mungall 2020).

Coarsening of boulders The relatively coarser grain size of the boulders may result from crystal ageing (Ostwald ripening), whereby larger crystals grow at the expense of smaller crystals (Voorhees 1985). Such a model has been proposed to explain pegmatoidal rocks associated with the UG2 chromitite (Cawthorn and Barry 2007), Merensky Reef (Cawthorn and Boerst 2006), and JM Reef (Jenkins et al. 2022). The lower portion of boulders is relatively coarser than the upper portions, which may arise from different cooling rates facilitated by the concentration of interstitial melts, particularly if the incongruent dissolution of pyroxene was pronounced at the base of boulders. In CSD profiles, Ostwald ripening is evidenced by convex-up profiles at smaller grain sizes and fanning profiles at larger grain sizes (Fig. 9). While our plagioclase CSD profiles (Fig. 9) are consistent with that expected from ripened grains, uncertainty, particularly at lower grain sizes, means that the operation of Ostwald ripening of plagioclase in the marginal zone cannot be empirically concluded.

Occurrence of olivine and chromite Chromite crystals occur within and along the bases of boulders, along sides and upper margins of boulders, and may extend laterally as chromitite seams into the host rocks (Maier and Barnes 2003).

Chromite crystals may occur as isolated grains (Figs. 4 and 5) or as chains surrounded by orthopyroxene, spatially associated with anhedral olivine (Fo_{91-82} ; cf. Yudovskaya et al. 2022). Nicholson and Mathez (1991) reported noritic inclusions within the Merensky pegmatoidal pyroxenite that were surrounded in turn by a ~1-cm-thick anorthosite and a <5 mm thick chromitite; similar sequences occur at the base of the Merensky cyclic unit (Smith et al. 2021) as well as within the Rum (O'Driscoll et al. 2009) and Stillwater (Marsh et al. 2021) complexes. Several models for the precipitation of anorthosite-associated chromitite seams have been proposed, many of which involve partial melting (O'Driscoll et al. 2009; Mathez and Kinzler 2017; Scoon and Costin 2018; Veksler and Hou 2020) or dissolution (Nicholson and Mathez 1991; Meurer et al. 1997; Baker and Boudreau 2019; Marsh et al. 2021) of ultramafic protocumulates. In either case, the partial incongruent melting (or dissolution) of orthopyroxene catalysed by evolved partial melts could form the observed forsteritic olivine and Cr-rich spinel concentrated at the bases of boulders (Shaw et al. 1998; Shaw and Dingwell 2008; Marsh et al. 2021). Such a process can account for other features reported in the marginal zone, including (i) the reverse zoning of marginal zone plagioclase at boulder bases, particularly the increase in intensity with proximity to the boulder-anorthosite reaction front (Schiffries 1982) and the preservation of compositional zoning (Robb and Mungall 2020); (ii) the relatively coarser grain size of the boulder bases; (iii) olivine-bearing boulders are associated with more calcic plagioclase (Jones 1976); (iii) the relative increase in amphibole, apatite, and phlogopite abundance (Figs. 6 and 7).

Sulfides and PGE contents of boulders Models of in situ crystallisation cannot explain the relatively high PGE concentrations of the Boulder Bed (Cu/Pd values < 1000; Maier and Barnes 2003). The PGE contents may instead have been inherited from a preexisting PGE-rich cumulate layer, of which there are many reported in the western lobe of the Bushveld Complex (Maier et al. 2013). Maier and Barnes (2003) noted that PGE and Au possess positive inter-element correlations (R^2 values > 0.7). Sulfur relatively poorly correlates with PGE contents (IPGE R^2 value = 0.43; PPGE R^2 value = 0.68), yet strongly positively correlates with Ni ($R^2 = 0.97$) and Cu ($R^2 = 0.98$). This suggests that PGE may be concentrated in discrete platinum-group minerals and spinel (Pagé et al. 2012), while Ni and Cu are controlled by sulfides. Sulfur and Cu may be preferentially removed during the incongruent dissolution of sulfides catalysed by an S-undersaturated phase, whereby Ni could be retained in residual mss-derived phases (pyrrhotite and pentlandite) or relocated to olivine (Peregoedova et al. 2004; Maier et al. 2021). During such a process, the PGE may concentrate in the residual sulfide (Kerr and Leitch 2005) and (or) undergo

desulfurisation to produce platinum-group minerals and alloys (Li and Ripley 2006). The distribution of chalcophile elements amongst boulders warrants further investigation.

Conclusion

The Boulder Bed of the western Bushveld Complex is an m-scale unit of mottled anorthosite containing sub-circular dm-scale 'boulders' of pyroxenite, harzburgite, and norite, occurring 10 s of metres below the Merensky Reef. Several petrogenetic models have been proposed for this enigmatic unit, which can be categorised as in situ and ex situ models. We propose that the boulders are the remains of a PGE-rich ultramafic layer that became dismembered during the heat- and (or) volatile-induced partial melting of the underlying (leuco)noritic cumulate rocks, which created an anorthosite restite. The upwelling partial melt reacted with the bases of boulders, which led to (i) the incongruent dissolution of cumulus orthopyroxene and crystallisation of unevolved anhedral olivine; (ii) the coarsening of the lower portions of boulders relative to the upper portions; (iii) precipitation of chromite; (iv) the increase in the intensity of reverse zoning in cumulus plagioclase with proximity to the boulder bases; (v) the presence of amphibole and late-stage silicates along the lower margins of some boulders; (vi) the dissolution of pre-existing base metal sulfides. Late-stage viscous compaction caused the partial flattening of boulders, where strain partitioned into intercumulus pyroxenes underlying the boulders. Given that magma replenishment, partial melting and (or) dissolution of proto-cumulates, and viscous compaction are likely common processes operating during the formation of layered intrusions, it remains unclear as to why boulders have not yet been described at other layered intrusions.

Supplementary Information The online version contains supplementary material available at <https://doi.org/10.1007/s00126-022-01150-y>.

Acknowledgements The DOI for the dataset "Electron Backscatter Diffraction (EBSD) Data for the Boulder Bed, Bushveld layered intrusion, South Africa." is <https://doi.org/10.17035/d.2022.0200189886>. This work would not have been possible without the provision of samples from Impala platinum mines (now Implats) and Rustenburg platinum mines to facilitate WDM's work on his PhD thesis in the late 1980s. Anthony Oldroyd is thanked for producing thick sections. Dr. Steve Barnes is thanked for providing micro-XRF maps and reviewing an earlier draft of this manuscript. Prof. David Reid is thanked for providing images of boulders in Fig. 2 from the Lonmin Marikana pit. Dr. Chris Jenkins' assistance helped improve the microtextural aspects of this contribution. Professors Georges Beaudoin and Marco Fiorentini are thanked for their editorial handling of this contribution. Insightful and kind reviews by Dr. Belinda Godel and Dr. Brian O'Driscoll helped improve an earlier version of this contribution.

Declarations

Conflict of interest The authors declare no competing interests.

References

- Allain-Bonasso N, Wagner F, Berbenni S, Field DP (2012) A study of the heterogeneity of plastic deformation in IF steel by EBSD. *Mater Sci Eng A* 548:56–63
- Armstrong JT (1995) Citzaf-a package of correction programs for the quantitative electron microbeam X-ray-analysis of thick polished materials, thin-films, and particles. *Microbeam Anal* 4:177–200
- Bachmann F, Hielscher R, Schaeben H (2010) Texture analysis with MTEX—free and open source software toolbox. In: *Solid state phenomena*, vol 160. Trans Tech Publications Ltd., pp 63–68
- Baker SR, Boudreau AE (2019) The influence of the thick banded series anorthosites on the crystallization of the surrounding rock of the Stillwater Complex, Montana. *Contrib to Mineral Petrol* 174:1–14
- Ballhaus CG, Cornelius M, Stumpfl EF (1988) The upper critical zone of the bushveld complex and the origin of merensky-type ores - a discussion. *Econ Geol* 83:1082–1085. <https://doi.org/10.2113/gsecongeo.83.5.1082>
- Barnes SJ, Taranovic V, Miller JM et al (2020) Sulfide emplacement and migration in the Nova-Bollinger Ni-Cu-Co deposit, Albany-Fraser orogen, Western Australia. *Econ Geol* 115:1749–1776
- Bennett EN, Lissenberg CJ, Cashman KV (2019) The significance of plagioclase textures in mid-ocean ridge basalt (Gakkal Ridge, Arctic Ocean). *Contrib Min Petrol* 174:1–22
- Bohrson WA, Spera FJ, Ghiorso MS et al (2014) Thermodynamic model for energy-constrained open-system evolution of crustal magma bodies undergoing simultaneous recharge, assimilation and crystallization: the magma chamber simulator. *J Petrol* 55:1685–1717
- Boorman S, Boudreau A, Kruger FJ (2004) The lower zone–critical zone transition of the Bushveld Complex: a quantitative textural study. *J Petrol* 45(6):1209–1235
- Boudreau AE (2019) Hydromagmatic processes and platinum-group element deposits in layered intrusions. Cambridge University Press
- Brewer LN, Field DP and Merriman CC (2009) Mapping and assessing plastic deformation using EBSD. *Electron backscatter diffraction in materials science*, pp 251–262
- Bunge H-J (2013) *Texture analysis in materials science: mathematical methods*. Elsevier
- Campbell IH, Naldrett AJ, Barnes SJ (1983) A model for the origin of the platinum-rich sulfide horizons in the Bushveld and Stillwater Complexes. *J Petrol* 24:133–165
- Cawthorn RG, Barry SD (1992) The role of intercumulus residua in the formation of pegmatoid associated with the UG2 chromitite, Bushveld Complex. *Aust J Earth Sci* 39:263–276
- Cawthorn RG, Boerst K (2006) Origin of the pegmatitic pyroxenite in the Merensky unit, Bushveld Complex, South Africa. *J Petrol* 47:1509–1530
- Cawthorn RG, Walraven F (1998) Emplacement and crystallization time for the Bushveld Complex. *J Petrol* 39(9):1669–1687
- Cawthorn RG, Latypov R, Klemm R, Vuthuza A (2018) Origin of discordant ultramafic pegmatites in the Bushveld Complex from externally-derived magmas. *South African J Geol* 2018(121):287–310
- Cheadle MJ, Gee JS (2017) Quantitative textural insights into the formation of gabbro in mafic intrusions. *Elem an Int Mag Mineral Geochem Petrol* 13:409–414
- Cousins CA (1969) The Merensky Reef of the Bushveld Igneous Complex. *Econ Geol Monograph* 4:239–251
- Eales HV, Cawthorn RG (1996) The bushveld complex. *Dev Petrol* 15:181–229 (Elsevier)
- Eales HV, Marsh JS, Mitchell AA et al (1986) Some geochemical constraints upon models for the crystallization of the upper critical zone–main zone interval, northwestern Bushveld complex. *Mineral Mag* 50:567–582
- Ferguson J, Botha E (1963) Some aspects of igneous layering in the basic zones of the Bushveld Complex. *S Afr J Geol* 66(1):259–282
- Hall AL (1924) On jade (massive garnet) from the Bushveld in the Western Transvaal. *S Afr J Geol* 27:49–55
- Heilbronner R, Tullis J (2002) The effect of static annealing on microstructures and crystallographic preferred orientations of quartzites experimentally deformed in axial compression and shear. *Geol Soc London, Spec Publ* 200:191–218
- Higgins MD (2002) A crystal size-distribution study of the Kiglapait layered mafic intrusion, Labrador, Canada: evidence for textural coarsening. *Contrib Miner Petrol* 144(3):314–330
- Higgins MD (2006) *Quantitative textural measurements in igneous and metamorphic petrology*. Cambridge University Press
- Holness MB, Hallworth MA, Woods A, Sides RE (2007) Infiltration metasomatism of cumulates by intrusive magma replenishment: the wavy horizon, Isle of Rum, Scotland. *J Petrol* 48:563–587
- Holness MB, Cawthorn RG, Roberts J (2017) The thickness of the crystal mush on the floor of the Bushveld magma chamber. *Contrib to Mineral Petrol* 172:102
- Holness MB, Morris C, Vukmanovic Z, Morgan DJ (2020) Insights into magma chamber processes from the relationship between fabric and grain shape in troctolitic cumulates. *Front Earth Sci* 8:352
- Humphreys MCS (2009) Chemical evolution of intercumulus liquid, as recorded in plagioclase overgrowth rims from the Skaergaard intrusion. *J Petrol* 50:127–145
- Hunter RH (1996) Texture development in cumulate rocks. In: *Developments in petrology*, vol 15. Elsevier, pp 77–101
- Jenkins MC, Mungall JE, Zientek ML, Butak K, Corson S, Holick P, McKinley R, Lowers H (2022) The geochemical and textural transition between the Reef Package and its hanging wall, Stillwater Complex, Montana, USA. *J Petrol* 63(7):egac053. <https://doi.org/10.5066/P9IHERKK>
- Jones JP (1976) Pegmatoidal nodules in the layered rocks of the Bafokeng leasehold area. *South African J Geol* 79:312–320
- Kerr A, Leitch AM (2005) Self-destructive sulfide segregation systems and the formation of high-grade magmatic ore deposits. *Econ Geol* 100:311–332
- Kinnaird JA (2005) *The Bushveld large igneous province*. The University of the Witwatersrand, Johannesburg, South Africa, Review Paper, p 39
- Lee CA, Sharpe MR (1980) Further examples of silicate liquid immiscibility and spherical aggregation in the Bushveld Complex. *Earth Planet Sci Lett* 48:131–147
- Leeb-Du Toit A (1986) The Impala platinum mines. In: *Mineral deposits of Southern Africa*, pp 1091–1106
- Li C, Ripley EM (2006) Formation of Pt-Fe alloy by desulfurization of Pt-Pd sulfide in the JM Reef of the Stillwater Complex, Montana. *Can Mineral* 44:895–903
- Maier W (1995) Olivine oikocrysts in Bushveld Anorthosite; some implications for cumulate formation. *Can Mineral* 33:1011–1022
- Maier WD, Barnes S-J (2003) Platinum-group elements in the Boulder Bed, western Bushveld Complex, South Africa. *Miner Depos* 38:370–380
- Maier WD, Eales HV (1997) Correlation within the UG2-Merensky Reef interval of the western Bushveld Complex. *Bull Geol Surv S Afr* 120:56
- Maier WD, Barnes SJ, Groves DI (2013) The Bushveld Complex, South Africa: formation of platinum–palladium, chrome-and vanadium-rich layers via hydrodynamic sorting of a mobilized

- cumulate slurry in a large, relatively slowly cooling, subsiding magma chamber. *Miner Deposita* 48(1):1–56
- Maier WD, Karykowski BT, Yang S-H (2016) Formation of transgressive anorthosite seams in the Bushveld Complex via tectonically induced mobilisation of plagioclase-rich crystal mushes. *Geosci Front* 7:875–889
- Maier WD, Barnes S-J, Muir D et al (2021) Formation of Bushveld anorthosite by reactive porous flow. *Contrib to Mineral Petrol* 176:1–12
- Mainprice D, Bachmann F, Hielscher R, Schaebe H (2015) Descriptive tools for the analysis of texture projects with large datasets using MTEX: strength, symmetry and components. *Geol Soc London, Spec Publ* 409:251–271
- Marsh BD (1988) Crystal size distribution (CSD) in rocks and the kinetics and dynamics of crystallization I. Theory *Contrib Mineral Petrol* 99:277–291
- Marsh JS, Pasieczny MJ, Boudreau AE (2021) Formation of chromitite seams and associated anorthosites in layered intrusion by reactive volatile-rich fluid infiltration. *J Petrol* 62(2):egaa109
- Mathez EA, Kinzler RJ (2017) Metasomatic chromitite seams in the Bushveld and Rum layered intrusions. *Elements* 13(6):397–402
- Meurer WP, Klüber S, Boudreau AE (1997) Discordant bodies from olivine-bearing zones III and IV of the Stillwater Complex, Montana—evidence for postcumulus fluid migration and reaction in layered intrusions. *Contrib to Mineral Petrol* 130:81–92
- Mungall JE, Kamo SL, McQuade S (2016) U-Pb geochronology documents out-of-sequence emplacement of ultramafic layers in the Bushveld Igneous Complex of South Africa. *Nat Commun* 7:1–13
- Naldrett AJ, Gasparrini EC, Barnes SJ et al (1986) The upper critical zone of the Bushveld Complex and the origin of Merensky-type ores. *Econ Geol* 81(5):1105–1117
- Naldrett AJ, Wilson AH, Kinnaird JA, Chunnett G (2009) PGE tenor and metal ratios within and below the Merensky Reef, Bushveld Complex : implications for its Genesis. *Am Mineral* 50:473–5064
- Naslund HR (1986) Disequilibrium partial melting and rheomorphic layer formation in the contact aureole of the Basistoppen sill, East Greenland. *Contrib Miner Petrol* 93(3):359–367
- Nicholson DM, Mathez EA (1991) Petrogenesis of the Merensky Reef in the Rustenburg section of the Bushveld Complex. *Contrib to Mineral Petrol* 107:293–309
- O'Driscoll B, Donaldson CH, Daly JS, Emeleus CH (2009) The roles of melt infiltration and cumulate assimilation in the formation of anorthosite and a Cr-spinel seam in the Rum Eastern Layered Intrusion. *NW Scotland Lithos* 111(1–2):6–20
- Pagé P, Barnes S-J, Bédard JHJ, Zientek ML (2012) In situ determination of Os, Ir, and Ru in chromites formed from komatiite, tholeiite and boninite magmas: implications for chromite control of Os, Ir and Ru during partial melting and crystal fractionation. *Chem Geol* 302:3–15
- Peregoedova A, Barnes S-J, Baker DR (2004) The formation of Pt–Ir alloys and Cu–Pd-rich sulfide melts by partial desulfurization of Fe–Ni–Cu sulfides: results of experiments and implications for natural systems. *Chem Geol* 208:247–264
- Piazolo S, Bestmann M, Prior DJ, Spiers CJ (2006) Temperature dependent grain boundary migration in deformed-then-annealed material: observations from experimentally deformed synthetic rocksalt. *Tectonophysics* 427:55–71
- Prichard HM, Barnes S-J, Godel BM et al (2015) The structure of and origin of nodular chromite from the Troodos ophiolite, Cyprus, revealed using high-resolution X-ray computed tomography and electron backscatter diffraction. *Lithos* 218:87–98
- Robb SJ, Mungall JE (2020) Testing emplacement models for the Rustenburg layered suite of the Bushveld Complex with numerical heat flow models and plagioclase geospeedometry. *Earth Planet Sci Lett* 534:116084
- Scoon RN, Costin G (2018) Chemistry, morphology and origin of magmatic-reaction chromite stringers associated with anorthosite in the upper critical zone at Winnaarshoek, Eastern Limb of the Bushveld Complex. *J Petrol* 59:1551–1578
- Scoon RN, Mitchell AA (2012) The upper zone of the Bushveld Complex at Roossenekal, South Africa: geochemical stratigraphy and evidence of multiple episodes of magma replenishment. *South African J Geol* 115:515–534
- Shaw CSJ, Dingwell DB (2008) Experimental peridotite–melt reaction at one atmosphere: a textural and chemical study. *Contrib to Mineral Petrol* 155:199–214
- Shaw CSJ, Thibault Y, Edgar AD, Lloyd FE (1998) Mechanisms of orthopyroxene dissolution in silica-undersaturated melts at 1 atmosphere and implications for the origin of silica-rich glass in mantle xenoliths. *Contrib to Mineral Petrol* 132:354–370
- Skemer P, Katayama I, Jiang Z, Karato S (2005) The misorientation index: development of a new method for calculating the strength of lattice-preferred orientation. *Tectonophysics* 411:157–167
- Smith WD, Maier WD (2021) The geotectonic setting, age and mineral deposit inventory of global layered intrusions. *Earth Sci Rev* 220:103736
- Smith WD, Maier WD, Barnes SJ et al (2021) Element mapping the Merensky Reef of the Bushveld Complex. *Geosci Front* 12(3):101101
- Veksler IV, Hou T (2020) Experimental study on the effects of H₂O upon crystallization in the lower and critical zones of the Bushveld Complex with an emphasis on chromitite formation. *Contrib Mineral Petrol* 175:1–17
- Vermaak CF (1976) The Merensky Reef thoughts on its environment and Genesis. *Econ Geol* 71:1270–1298
- Vigneress JL, Tikoff B (1999) Strain partitioning during partial melting and crystallizing felsic magmas. *Tectonophysics* 312:117–132
- Viljoen MJ, Hieber R (1986) The Rustenburg Section of Rustenburg Platinum Mines Limited, with reference to the Merensky Reef. In: Anhaeusser CR, Maske S (eds) *Mineral deposits of South Africa*. Geological Society of South Africa, Johannesburg, pp 1107–1134
- Voorhees PW (1985) The theory of Ostwald ripening. *J Stat Phys* 38:231–252
- Vukmanovic Z, Holness MB, Stock MJ, Roberts RJ (2019) The creation and evolution of crystal mush in the upper zone of the Rustenburg Layered Suite, Bushveld Complex, South Africa. *J Petrol* 60:1523–1542
- Yao Z, Mungall JE, Jenkins MC (2021) The Rustenburg Layered Suite formed as a stack of mush with transient magma chambers. *Nat Commun* 12(1):1–13
- Yudovskaya MA, Kinnaird JA, Costin G, McCreech M, Shilovskikh V, Kovalchuk E, Kuzmin D (2022) Formation of spinel-orthopyroxene symplectites by reactive melt flow: examples from the northern Bushveld Complex and implications for mineralization in layered intrusions. *Econ Geol*. <https://doi.org/10.5382/econgeo.4938>

Publisher's note Springer Nature remains neutral with regard to jurisdictional claims in published maps and institutional affiliations.

Springer Nature or its licensor (e.g. a society or other partner) holds exclusive rights to this article under a publishing agreement with the author(s) or other rightsholder(s); author self-archiving of the accepted manuscript version of this article is solely governed by the terms of such publishing agreement and applicable law.